Available online at www.sciencedirect.com
ScienceDirect
Comput. Methods Appl. Mech. Engrg. 396 (2022) 115099
Computer methods in applied mechanics and engineering
www.elsevier.com/locate/cma

An immersed MMALE material point method for FSI problems with structure fracturing[☆]

Lei Kan, Xiong Zhang[*]

School of Aerospace Engineering, Tsinghua University, Beijing 100084, PR China

Received 19 January 2022; received in revised form 15 April 2022; accepted 30 April 2022
Available online xxxx

Abstract

The fluid–structure-interaction (FSI) modeling is important for both academic studies and engineering applications, but is also one of the grand challenges in the numerical modeling community. The FSI problems with multi-material fluid flow and extreme structure deformation accompanied with fractures and crack growth are less explored areas. In these problems, the interface reconstruction, multi-material advection, interface interaction on the complicated fluid structure interface and potential structure fragmentation must be all taken into account. This paper aims to present an effective monolithic approach of immersed multi-material arbitrary Lagrangian Eulerian material point method (IALEMPM) by immersing the MPM particles in the MMALE grid. In this novel method, the interfaces between the fluid and structure are tracked implicitly by the MPM particles and the interface interactions are implicitly implemented by assembling the nodal force and the nodal momentum from both the solid particles and fluid cells. The consistence time integration scheme, rezoning phase and remapping phase are also established to guarantee the consistence requirements during the whole simulation. Numerical examples, including a shock-obstacle interaction, a blast-plate interaction and a structure fragmentation are studied by using the IALEMPM, and all the numerical results show good agreement with the benchmark and the experiment data, which indicates that the IALEMPM is effective for solving these complicated FSI problems.

Keywords: Material point method; Multi-material arbitrary Lagrangian Eulerian method; Fluid–structure interaction; Monolithic approach

---

1. Introduction

Fluid–structure-interaction (FSI) is a common phenomenon in nature and widely exists in engineering fields. It is important to figure out the mechanism of the physical phenomenon related to FSI or summarize physical laws for engineering applications. Many researchers use numerical simulations to study FSI problems ranging in porous media [1,2], blood flow [3], atmospheric turbulent flows over environmental terrains [4], nuclear [5], sailing of marine vessels [6] and parachutes [7–10]. Numerical simulation methods have already made remarkable progress in dealing with the non-extreme problems. However, FSI problems with multi-material fluid flow and extreme structure deformation accompanied with fractures and crack growth are less explored areas. The accurate simulation to these

---

[☆] Supported by the National Natural Science Foundation of China (12172192).

[*] Corresponding author.
E-mail address: xzhang@tsinghua.edu.cn (X. Zhang).

https://doi.org/10.1016/j.cma.2022.115099

phenomena is of great significance in the area of architecture explosive defense, weapon damage capability analysis and airfoil design. In these problems, the difficulty mainly lies in complicated two-way fluid–structure interaction at the fluid–structure interfaces which may become distorted or fragmented due to the large deformation and potential fracturing of the structure. The large discrepancy of material behaviors between the nonlinear plastic solid and the multi-material fluid imposes an additional challenge.

The coupling of the mesh-based methods such as the finite element method (FEM), finite difference method (FDM) or finite volume method (FVM) is still the most common techniques to establish FSI simulation method. According to different handling methods of fluid–structure coupling interface boundary, Kim and Choi [11] grouped the modeling methodologies into two main categories. The first category encapsulates the methods where the fluid mesh conforms to the solid boundaries, while the second category groups all the methods where there are overlaps between the fluid and the solid meshes. Interface-tracking methods such as the arbitrary Lagrangian–Eulerian (ALE) method [12–14] and space–time methods [15–17] are the typical representative of the first category. The conformal meshing could accurately track the fluid structure interfaces with relatively coarse mesh, however, the remeshing and remapping techniques are required to maintain the quality of elements as the mesh deforms. Furthermore, the conformal property of the mesh could terminate the calculation when the interfaces are distorted. In the another FSI methodology, the mesh does not conform to the structural domain. Immersed boundary method [18], cut-cell method [19], and level-set methods [20] solve the fluid problem on a fixed Eulerian mesh with respective special interface algorithm. Such techniques require a more refined mesh for resolving the interface, satisfying the interface conditions, and capturing the boundary layer. The immersed boundary method (IB) originally proposed by Peskin [18] in the 1970s was to study the flow patterns around the valves. Based on the immersed method, other formulations were proposed like immersed finite element method (IFEM) proposed by Zhang et al. [21,22] and immersed smoothed finite element method (IS-FEM) [23] for the solution of the interaction problems between the complex fluid flow in fixed grid and deformable finite element structure. The term “immersed” indicates that the structure is submerged in the entire fluid domain and interaction between fluid and structure is accomplished by distributing the nodal forces and interpolating the velocities between Eulerian and Lagrangian domains. The advantage of the IB method is embodied in that the fluid–structure interface is tracked automatically with a relatively simple cartesian mesh configuration which is more effective. Therefore, immersed method is suitable to solve FSI problems with complex fluid structure interfaces. The mesh-based methods have made profound progress in the modeling of massive problems such as the incompressible flow [24], weakly compressible flow with nonlinear elastic solid [25] and the FSI with thickless flexible bodies [26] at high accuracy, stability and efficiency. However the mesh-based methods which rely upon the topological grid to discretize the domain are not well suited in modeling large deformation and massive fracture generating and extending.

Since the 1970s, efforts have been underway to seek better alternatives to overcome limitations of mesh-based formulations. With the development of numerical methodologies, the mesh-free methods have been found to provide an efficient and accurate solution for many practical problems. The mesh-free methods, such as the smoothed particle hydrodynamics (SPH) [27], element-free Galerkin method (EFGM) [28], reproducing kernel particle method (RKPM) [29], material point method (MPM) [30], and peridynamics (PD) [31] are considered to be better suited for solving problems involving moving boundaries, large deformation, structure failure and crack growth. The remarkable capabilities of mesh-free methods in modeling nonlinear fluid and solid problems have motivated computational community to solve FSI problems employing mesh-free methods. Because all the mesh-free methods discretize the domain with particles which carry the physical information and solve the control equation by the particle interaction, the coupling of mesh-free method for FSI algorithm is directive. Han and Hu [32] proposed a SPH modeling of FSI interaction by combining a transport-velocity SPH scheme which advances fluid motions with a total Lagrangian SPH formulation to deal with the structure deformations and Zhang et al. [33] proposed a Riemann-SPH method to simulate hydroelastic fluid–structure interaction (FSI) problems. The SPH method has also been coupled with newly developed PD to modeling fracture in the FSI [34,35]. For the other mesh-free methods, Soga et al. [2] used the MPM to simulate FSI problem of soil deformation where two sets of MPM particles are considered to represent soil skeleton and pore water layers. Nevertheless, it is still hard for the mesh-free method to precisely simulate the compressible fluid flow with shock wave.

Hence, in order to take advantages of the high accuracy of mesh-based method in fluid and the ability to simulate large deformation of mesh-free method in solid, technologies to couple the two method have been proposed. Gilmanov et al. [36] developed a hybrid immersed boundary and material point method for solving the 3D, unsteady, incompressible Navier–Stokes equations in curvilinear coordinates. Yu et al. [37] also adopted an immersed method to form a hybrid meshfree-Cartesian scheme with mesh-free particles to model large deformation of solid in the Cartesian described fluid domain. Zheng et al. [38] coupled the lattice Boltzmann and material point method for fluid–solid interaction problems involving massive deformation. Shimada et al. [39] proposed a monolithic method that uses the cell-centered finite volume formulation in the Eulerian description and the Lagrangian marker particles in the solid region to establish an incompressible mixture formulation. However, few method has explored the area of the compressible fluid with multiple materials and the structure with nonlinear material property (like plasticity), large deformation and fractures, which is the main target of our work.

For the large deformation and potential fracturing in the structure, the material point method (MPM) provides a powerful tool. The MPM is a kind of hybrid Lagrangian and Eulerian method. The domain is discretized by Lagrangian particles which carry the motion, deformation and constitutive information (such as stress, strain, internal energy and stress history). In each time step, the information on the particles is projected to the background grid to solve the weak form of momentum equation. The updated Lagrangian mesh momentum is then remapped back to particles to update their state variables, and the background grid is reset to its initial state. Hence, the background grid performs like an Eulerian mesh which avoids mesh distortion and element entanglement. The MPM has been applied in modeling many extreme events, such as hyper velocity impact [40,41], penetration [42], explosion [43], fracture evolution [44–47], fluid–structure interaction [36,48,49]. For the compressible flow with multiple materials, the multi-material arbitrary Lagrangian Eulerian method (MMALE) [50–52] is a suitable choice. The MMALE was originally proposed to solve fluids with multiple materials without tracking the complicated material interfaces. It introduces multi-material cells to allow multiple materials attending in a single cell, which makes MMALE superior in simulating complicated compressible flow in 3D with pure or multiple materials. The MMALE is successful in simulation of multi-material compressible flow due to its high accuracy and precisely tracing of the material interface. The MMALE also adopts a hybrid Lagrangian and Eulerian description of indirect ALE [53] which consists of three phases, a Lagrangian phase [54,55] in which the physical variables and mesh are updated, a rezoning phase for defining a new mesh with better quality, and a remapping phase [52,56] wherein the physical variables are conservatively interpolated from the old Lagrangian mesh onto the newly rezoned one. It is inspiring that the MPM and MMALE are analogical, where both of them consist of Lagrangian momentum updating and Eulerian remeshing. Therefore, by applying the aforementioned immersed method to submerge the MPM particles in MMALE grid, the MPM is coupled with MMALE to establish a monolithic FSI algorithm named immersed multi-material arbitrary Lagrangian Eulerian material point method (IALEMPM). The monolithic formulation makes the complicated fluid–structure interaction in extreme problems be implemented implicitly, so that the IALEMPM is effective for solving complicated FSI problems with multi-material compressible fluid flow and extreme structure deformation and fracturing.

The remaining part of the paper is organized as follows. In Section 2, the basic idea of the MMALE and MPM is briefly reviewed with emphasis on their similarity. Section 3 presents the detailed formation of the proposed IALEMPM including the Lagrangian step, the rezoning phase and the remapping phase. Numerical results on several benchmark problems are given in Section 4. Finally Section 5 gives the conclusion.

2. Brief review of the MMALE and MPM method

Both the MMALE and MPM employ the Lagrangian method to solve the governing equations. The governing equations of continuum mechanics in the updated Lagrangian frame are

$$\frac{\mathrm{d}\rho}{\mathrm{d}t} = -\rho v_{i,i} \tag{1}$$

$$\rho\frac{\mathrm{d}v_i}{\mathrm{d}t} = \sigma_{ij,j} + \rho b_i \tag{2}$$

$$\rho\frac{\mathrm{d}e}{\mathrm{d}t} = \dot{\varepsilon}_{ij}\sigma_{ij} \tag{3}$$

where ρ is the current density, e is the specific internal energy, the subscripts i and j indicate the components of the spatial variables following the Einstein convention, v_i is the velocity, b_i is the body force per unit mass, σ_{ij} is the Cauchy stress, ε_{ij} is the Cauchy strain. Note that the comma in the subscript denotes the derivative.

The weak form equivalent to the momentum equation (2) and the traction boundary condition is given as

$$\int_{\Omega} \rho \ddot{u}_i \delta u_i \mathrm{d}\Omega + \int_{\Omega} \rho \sigma_{ij}^s \delta u_{i,j} \mathrm{d}\Omega - \int_{\Omega} \rho b_i \delta u_i \mathrm{d}\Omega - \int_{\Gamma_t} \rho \bar{t}_i^s \delta u_i \mathrm{d}\Gamma = 0 \tag{4}$$

where Γ_t denotes the traction boundary of the material domain Ω, $\sigma_{ij}^s = \sigma_{ij}/\rho$ is the specific stress, $\bar{t}_i^s = \bar{t}_i/\rho$ is the specific traction, $\bar{t}_i$ is the traction, u_i is the displacement and δu_i is the virtual displacement.

The displacement field can be approximated as

$$u_i(\boldsymbol{x}) = N^I(\boldsymbol{x}) u_i^I \tag{5}$$

where the superscript I denotes the variables associated with the grid node I following the Einstein convention, $N^I(\boldsymbol{x})$ denotes the grid nodal shape function, u_i^I is the grid nodal displacement and $\boldsymbol{x}$ is the coordinate in the current configuration.

Substituting Eq. (5) into the weak form equation (4) and invoking the arbitrariness of the virtual displacement δu_i^I leads to the grid nodal momentum equation

$$\dot{p}_i^I = f_i^I + \tilde{f}_i^I, \quad \forall I \notin \Gamma_u \tag{6}$$

where Γ_u is the displacement boundary of the material domain,

$$p_i^I = m^I \dot{u}_i^I \tag{7}$$

is the grid nodal momentum,

$$m^I = \int_{\Omega} \rho N^I(\boldsymbol{x}) \mathrm{d}\Omega \tag{8}$$

is the lumped grid nodal mass,

$$f_i^I = -\int_{\Omega} N_{,j}^I(\boldsymbol{x}) \sigma_{ij} \mathrm{d}\Omega \tag{9}$$

is the internal nodal force,

$$\tilde{f}_i^I = \int_{\Omega} \rho b_i N^I(\boldsymbol{x}) \mathrm{d}\Omega + \int_{\Gamma_t} N^I(\boldsymbol{x}) \bar{t}_i \mathrm{d}\Gamma \tag{10}$$

is the external nodal force. In Eq. (7), the consistent grid nodal mass is replaced by the lumped grid nodal mass to significantly reduce the computational cost of the explicit integration.

The momentum equation equation (6) is solved by different spatial discretization in the MMALE and MPM.

2.1. The MMALE method for fluid

As aforementioned, the MMALE method consists of a Lagrangian phase, a rezoning phase and a remapping phase.

2.1.1. Lagrangian phase

In the Lagrangian phase, the computational frame follows the material motion. Many efforts have been devoted to develop an accurate, stable and robust formulation to simulate the behavior of fluid in the Lagrangian frame. The compatible discretization scheme [55,57] is one of the most important Lagrangian schemes. It employs the staggered discretization, in which the position and velocity are located at the nodes while other variables such as density, internal energy, pressure and sound speed are cell-centered.

Spatial discretization. Fig. 1 shows a 2D staggered grid discretization of four cells, in which each cell is divided into four corner volumes. The characters c and I respectively denote the cell and node, and Ω_c^I denotes the sub-cell domain in the cell c at the corner of node I. The subscripts of c and I denote the serial number. The controlling domain of a node is defined as the summation of the connected corner domains, namely,

$$\Omega^I = \sum_c \Omega_c^I \tag{11}$$

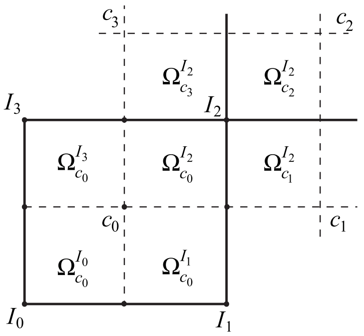

Fig. 1. The spatial discretization of staggered grid.

and also the cell domain can be represented by

$$\Omega_c = \sum_I \Omega_c^I \tag{12}$$

The density is stored in cell center and denoted as ρ_c. Thus, the corner mass m_c^I can be obtained as

$$m_c^I = \rho_c V_c^I \tag{13}$$

where V_c^I is the corner volume of the sub-cell domain Ω_c^I. By summing up the corner mass around a node or in a cell, the nodal mass m^I and cell mass m_c can be calculated as

$$m^I = \sum_{\Omega_c^I \in \Omega^I} m_c^I, \quad m_c = \sum_{\Omega_c^I \in \Omega_c} m_c^I \tag{14}$$

The nodal mass defined in Eq. (14) is an approximation to Eq. (8) and is treated as a constant value in the Lagrangian phase. This treatment can reduce the computational time consumption and eliminate the spurious grid distortion and the resultant grid tangling [55]. The volume of sub-cell domain in 3D can be calculated by cutting the hexahedron into six tetrahedrons and summing up their volumes [57].

Then substituting the stress tensor $\sigma_{ij} = -P\delta_{ij}$ into the momentum conservation law equation (2) gives

$$\rho \frac{\mathrm{d}v_i}{\mathrm{d}t} = -P_{,i} + \rho b_i \tag{15}$$

where P denotes the pressure and δ_{ij} denotes the Kronecker delta. Integrating Eq. (15) on the support domain Ω^I and applying the Gauss's theory lead to the discretized momentum equation

$$m^I \ddot{u}_i^I = -\sum_c \int_{\Gamma_c^I} P n_i \mathrm{d}\Gamma + m^I b_i^I + \int_{\Gamma_t^I} \bar{t}_i \mathrm{d}\Gamma = f_i^I + \tilde{f}_i^I \tag{16}$$

where n_i denotes the normal vector, Γ_c^I denotes the inner surfaces of sub-cell Ω_c^I, Γ_t^I denotes the force boundary in the support of the node I,

$$f_i^I = \sum_c f_{ci}^I = -\sum_c P_c^I \int_{\Gamma_c^I} n_i \mathrm{d}\Gamma \tag{17}$$

$$\tilde{f}_i^I = m^I b_i^I + \int_{\Gamma_t^I} \bar{t}_i \mathrm{d}\Gamma \tag{18}$$

where f_{ci}^I is the corner force of the sub-cell Ω_c^I in the ith direction.

The internal energy equation (3) can also be rewritten as

$$\rho \frac{\mathrm{d}e}{\mathrm{d}t} = -P v_{i,i} \tag{19}$$

Substituting Eq. (16) into Eq. (19) and applying the energy conservation law of the whole system result in the internal energy semi-discrete scheme [57]

$$m_c \frac{\mathrm{d}e_c}{\mathrm{d}t} = -\sum_I v_i^I f_{ci}^I \tag{20}$$

It should be emphasized that the discretization of the momentum and energy equations is compatible because the energy conservation of the system can be rigorously preserved. The total energy Φ consists of total internal energy and kinetic energy, namely

$$\Phi = \sum_c m_c e_c + \sum_I \frac{1}{2} m^I v_i^I v_i^I$$

The derivative of Φ is given as

$$\begin{aligned}
\frac{\mathrm{d}\Phi}{\mathrm{d}t} &= \sum_c m_c \frac{\mathrm{d}e_c}{\mathrm{d}t} + \sum_I m^I v_i^I \frac{\mathrm{d}v_i^I}{\mathrm{d}t} \\
&= \sum_c m_c \frac{\mathrm{d}e_c}{\mathrm{d}t} + \sum_I \sum_c v_i^I f_{ci}^I + \sum_I v_i^I \tilde{f}_i^I \\
&= \sum_c \Big(m_c \frac{\mathrm{d}e_c}{\mathrm{d}t} + \sum_I v_i^I f_{ci}^I\Big) + \sum_I v_i^I \tilde{f}_i^I \\
&= \sum_I v_i^I \tilde{f}_i^I
\end{aligned}$$

where the momentum equations (16), (17) and internal energy discrete equation (20) are substituted. In the equation above, the total energy is only related to the external force $\tilde{f}_i^I$, which indicates that the energy conservation of the system can be rigorously preserved. Therefore, Eqs. (16) and (20) are termed as the “compatible discretization”.

Time integration. The predictor–corrector scheme [58] is used for the time integration. In the predictor step, a temporary grid is updated to the half-step $k + 1/2$ first as

$$u_i^{I,k+1/2} = u_i^{I,k} + \frac{1}{2} v_i^{I,k} \Delta t \tag{21}$$

$$V_c^{k+1/2} = V(u_i^{I,k+1/2}) \tag{22}$$

where $V(u_i^{I,k+1/2})$ denotes the cell volume at the half-step, and the comma in the superscript separates the time index from spatial index. The volume $V(u_i^{I,k+1/2})$ is calculated by the positions of nodes at the half-step $x_i^{I,k+1/2}$ in the cell. Then the pressure $P_c^{k+1/2}$ can be calculated by an isentropic hypothesis as

$$P_c^{k+1/2} = P_c^k - \rho_c^k (\kappa_c^k)^2 \frac{V_c^{k+1/2} - V_c^k}{V_c^k} \tag{23}$$

where κ denotes the adiabatic sound velocity and is calculated according to the equation of state. Substituting the temporary pressure $P_c^{k+1/2}$ to Eq. (16) and applying the force boundary, the nodal acceleration of the half-step is obtained as

$$a_i^{I,k+1/2} = \frac{f_i^{I,k+1/2} + \tilde{f}_i^{I,k+1/2}}{m^I} \tag{24}$$

where a denotes the acceleration.

For the corrector step, the grid of the next step is calculated by the temporary force and acceleration, namely,

$$v_i^{I,k+1} = v_i^{I,k} + a_i^{I,k+1/2} \Delta t \tag{25}$$

$$v_i^{I,k+1/2} = \frac{1}{2}(v_i^{I,k} + v_i^{I,k+1}) \tag{26}$$

$$u_i^{I,k+1} = u_i^{I,k} + v_i^{I,k+1/2} \Delta t \tag{27}$$

$$V_c^{k+1} = V(u_i^{I,k+1}) \tag{28}$$

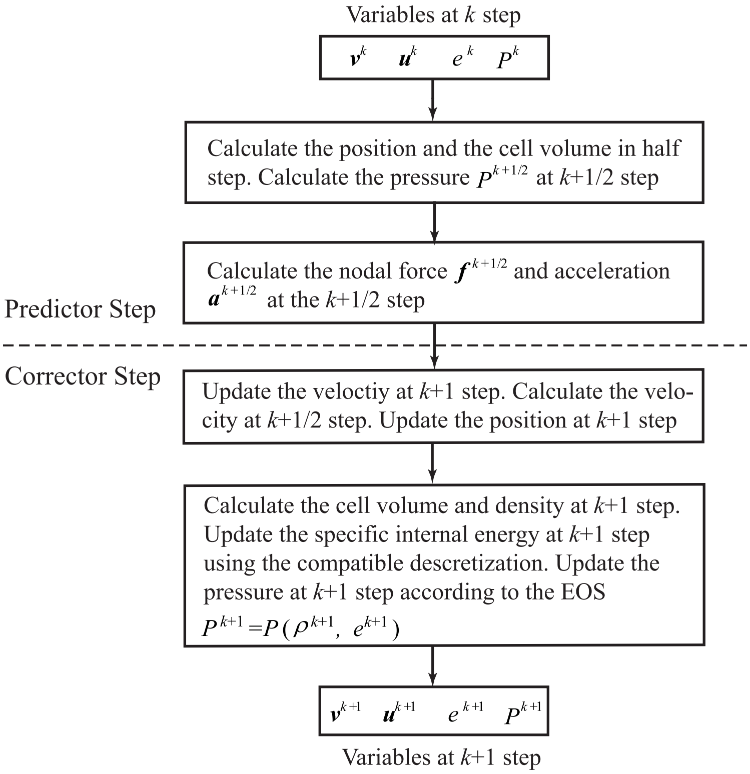

Fig. 2. Flow chart of the MMALE.

The cell centered density, specific internal energy and pressure are updated by the volume, energy conservation law and the equation of state, respectively, namely

$$\rho_c^{k+1} = m_c / V_c^{k+1} \tag{29}$$

$$m_c \frac{e_c^{k+1} - e_c^k}{\Delta t} = -\sum_I f_{c,i}^{I,k+1/2} v_i^{I,k+1/2} \tag{30}$$

$$P_c^{k+1} = P(\rho_c^{k+1}, e_c^{k+1}) \tag{31}$$

where $P(\rho_c^{k+1}, e_c^{k+1})$ denotes the function of the equation of state of the fluid, and it is used to update the pressure according to the density and specific internal energy.

A flow chart of the solution scheme is briefly illustrated in Fig. 2.

The artificial viscosity is very important to be applied to provide the entropy production and introduce dissipation for shock discontinuity, and a large number of artificial viscosity schemes have been proposed. In this paper, a tensor finite element viscosity and an edge viscosity are applied [59,60]. Since the pressure, energy and density are stored in the cell center in the staggered grid, the Lagrangian step essentially adopts the one-point Gaussian quadrature. Hence, an hourglass viscosity is also needed to eliminate the hourglass motion and spurious vorticity [61].

For the multi-material cells where the cell is composed of multiple materials in the MMALE, the material portion can be represented by material volume fraction η_l and material centroid ξ_{li}, where the subscript l denotes the lth material. The density, pressure and specific energy of each material are also carried by the cell center as ρ_l, P_l and e_l, respectively. A closure model [62–65] is needed to derive multi-material element pressure to form the corner force and to formulate the updating scheme of the material internal energy and pressure. The Tipton pressure relaxation model [65] is the most popular one and used in this paper. Additionally, the material centroid should also be updated in the Lagrangian phase for the material interface reconstruction and a constant parametric coordinate method [66] is a convenient choice.

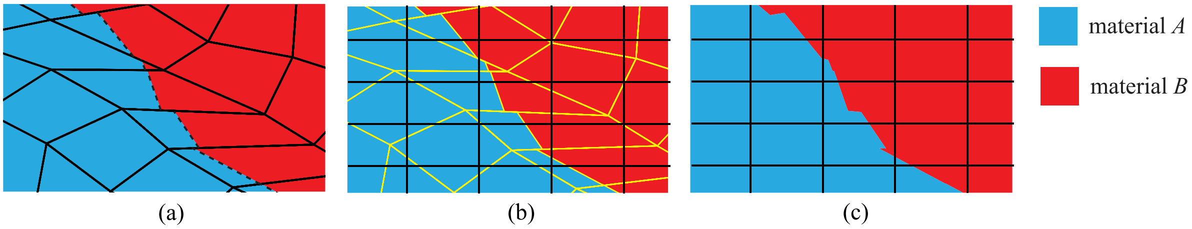

Fig. 3. Remapping process of MMALE [52]. (For interpretation of the references to color in this figure legend, the reader is referred to the web version of this article.)

2.1.2. Rezoning phase

In the rezoning phase, the new mesh with higher quality replaces the distorted old mesh. Two critical problems which should be solved in this phase are when and how to rezone the mesh. For the first one, the grid can be judged distorted when the shape of the cell is distorted [50] or the average node displacement between two Lagrangian step is quite small [51]. And for the other problem, in the tradition ALE scheme where the rezoned mesh is required to conform the material interface, the rezoning scheme is still difficult and time-consuming. However, under the formulation of the MMALE which allows the material interface pass through the cell and adopts a cell-intersection based remapping method, the difficulties in the rezoning phase are avoided in essence because the location of the material interface does not affect the rezoning phase any more. Some rezoning scheme can be found in the literature [50,67], while the simplest scheme for structured regular hexahedron grid is to reset the distorted old grid to its initial position.

2.1.3. Remapping phase

The purpose of the remapping phase is to determine the physical variables, including density, internal energy, material volume fraction, material centroid and velocity in the new grid generated by the rezoning phase.

As illustrated in Fig. 3, the multi-material remapping phase consists of three steps [52]: (a) reconstruct the material surfaces (dashed lines) of the distorted grid (black solid lines) between the material A (in blue) and material B (in red) by an interface reconstruction scheme, so that the original multi-material cells are cut into separated polyhedrons of pure material (black lines). (b) Intersect the rezoned grid (black lines) with the material polyhedrons (yellow lines) to obtain the intersection pieces. (c) Accumulate the physical variables of all intersection pieces in a new cell to obtain the physical variables of the new cell.

Piecewise Linear Interface Calculation (PLIC) is a commonly used method for constructing fluid interfaces in multi-material cells based on the volume fraction of each fluid in each cell. In this paper, the moment of fluid (MoF) method [68–70] is used to reconstruct fluid interfaces. Compared with the traditional PLIC-VoF method [66], the MoF does not need any information from the neighbor cells, which allows it to be implemented as a cell-by-cell black-box routine and be parallelized innately. The MoF constructs a fluid interface by precisely matching the materials' volume and minimizing the discrepancy between the given reference materials' centroid and the reconstructed materials' centroid. Namely, the MoF determines a particular plane $\boldsymbol{n} \cdot \boldsymbol{x} + d = 0$ to minimize the objective function

$$f(\boldsymbol{n}, d) = \|\boldsymbol{\xi}(\boldsymbol{n}, d) - \boldsymbol{\xi}^{\mathrm{ref}}\|^2 \tag{32}$$

subject to the volume condition

$$V(\boldsymbol{n}, d) = V^{\mathrm{ref}} \tag{33}$$

where $\boldsymbol{n}$ and d denote the parameters of the reconstructed plane, and $\boldsymbol{\xi}(\boldsymbol{n}, d)$ and $V(\boldsymbol{n}, d)$ are the centroid and volume below the truncation polyhedron by the reconstructed interface, respectively. $\boldsymbol{\xi}^{\mathrm{ref}}$ and V^{ref} are respectively the given reference material centroid and volume in the multi-material cell. The reference volume and centroid here are actually the volume and centroid of the material in the multi-material cell and are updated in the Lagrangian phase. The referenced volume is obtained from the volume fraction. If the material l is chosen to be the target, the reference volume is given as, $V^{\mathrm{ref}} = \eta_l V$. The referenced centroid $\boldsymbol{\xi}(\boldsymbol{n}, d)$ of each material is stored in the cell center and its natural coordinates are assumed to be constant in the Lagrangian phase. This approximation is proved valid by Kucharik et al. [66].

After the interface reconstruction process, the old grid is decomposed into non-overlapping polyhedrons and each polyhedron only contains one material, which is termed as the material polyhedron. For the pure material cell, no interface reconstruction is carried out and the whole cell is treated as a material polyhedron. The variables for every material are interpolated to the material polyhedrons and then the variable remapping calculation is conducted.

The intersection based remapping method [51,52,71] relieves the aforementioned limitations of the rezoning phase and is widely used to interpolate the volume fraction and the material centroid in MMALE to avoid the unphysical phenomena like negative mass and pseudo fragmentation [72]. In the intersection based method, every cell in the new grid intersects with the material polyhedrons in the old grid.

To remap the cell-centered variables ρ_{cl}, e_{cl}, V_c, η_l and ξ_{li}, the cell volume and the mass, internal energy, volume, and the moment of the lth material in the cell c of the new grid are first accumulated by intersecting with cells of the old grid as

$$\tilde{V}_c = \sum_t \int_{\Omega(H_t \cap \tilde{\Omega}_c)} \mathrm{d}\Omega, \;\; t \in \{t \mid H_t \cap \tilde{\Omega}_c \neq \emptyset\} \tag{34}$$

$$\tilde{m}_{cl} = \sum_t \int_{\Omega(H_t \cap \tilde{\Omega}_c)} \rho \mathrm{d}\Omega, \;\; t \in \{t \mid H_t \cap \tilde{\Omega}_c \neq \emptyset, \; H_t \in \mathscr{H}_l\} \tag{35}$$

$$\tilde{E}_{cl} = \sum_t \int_{\Omega(H_t \cap \tilde{\Omega}_c)} \rho e \mathrm{d}\Omega, \;\; t \in \{t \mid H_t \cap \tilde{\Omega}_c \neq \emptyset, \; H_t \in \mathscr{H}_l\} \tag{36}$$

$$\tilde{V}_{cl} = \sum_t \int_{\Omega(H_t \cap \tilde{\Omega}_c)} \mathrm{d}\Omega, \;\; t \in \{t \mid H_t \cap \tilde{\Omega}_c \neq \emptyset, \; H_t \in \mathscr{H}_l\} \tag{37}$$

$$\tilde{M}_{cli} = \sum_t \int_{\Omega(H_t \cap \tilde{\Omega}_c)} x_i \mathrm{d}\Omega, \;\; t \in \{t \mid H_t \cap \tilde{\Omega}_c \neq \emptyset, \; H_t \in \mathscr{H}_l\} \tag{38}$$

where $\tilde{\Omega}_c$ denotes the cell c of the new grid, H_t denotes the polyhedron t in the old grid. $\Omega(H_t \cap \tilde{\Omega}_c)$ is the intersected domain of the new grid cell c and the polyhedron t in the old grid. $\tilde{E}_{cl}$, $\tilde{m}_{cl}$, $\tilde{V}_{cl}$ and $\tilde{M}_{cli}$ denote the internal energy, mass, volume and moment of the lth material in the cth cell of the new grid, and $\mathscr{H}_l$ denotes the set of all the polyhedrons of the lth material. Note that the field of the density ρ and internal energy per volume ρe in the above equations in each cell are obtained by linear reconstruction from the surrounding 26 cell centers with the least square method to ensure the second-order accuracy.

Subsequently, the density $\tilde{\rho}_{cl}$, specific internal energy $\tilde{e}_{cl}$, the volume fraction $\tilde{\eta}_{cl}$ and the centroid $\tilde{\xi}_{cli}$ of the material l in the new grid cell c are given as

$$\tilde{\rho}_{cl} = \tilde{m}_{cl} / \tilde{V}_{cl} \tag{39}$$

$$\tilde{e}_{cl} = \tilde{E}_{cl} / \tilde{m}_{cl} \tag{40}$$

$$\tilde{\eta}_{cl} = \tilde{V}_{cl} / \tilde{V}_c \tag{41}$$

$$\tilde{\xi}_{cli} = \tilde{M}_{cli} / \tilde{V}_{cl} \tag{42}$$

For the nodal velocity $\tilde{v}_i^I$, the nodal momentum and mass are accumulated first by intersecting the controlling domains between new nodes and the old nodes, namely,

$$\tilde{m}^I = \sum_t \rho_t \int_{\Omega(H_t \cap \tilde{\Omega}_c)} \mathrm{d}\Omega, \;\; t \in \{t \mid H_t \cap \tilde{\Omega}^I \neq \emptyset\} \tag{43}$$

$$\tilde{p}_i^I = \sum_t v_{ti} \rho_t \int_{\Omega(H_t \cap \tilde{\Omega}_c)} \mathrm{d}\Omega, \;\; t \in \{t \mid H_t \cap \tilde{\Omega}^I \neq \emptyset\} \tag{44}$$

where $\tilde{\Omega}^I$ is the support domain of Ith node in the new grid, v_{ti} is the velocity of polyhedron t obtained by interpolation and ρ_t denote the polyhedron density. Subsequently, the node velocity in the new grid is

$$\tilde{v}_i^I = \frac{\tilde{p}_i^I}{\tilde{m}^I} \tag{45}$$

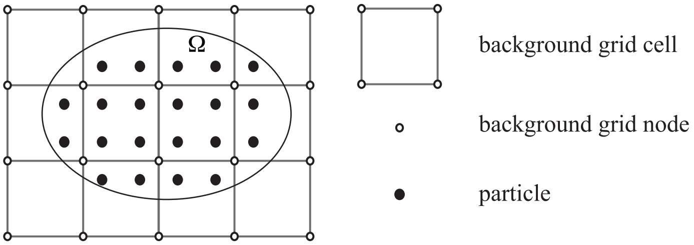

Fig. 4. The spatial discretization of the MPM.

After these two steps, the variables have been remapped to the newly rezoned grid from the old grid. Another round of Lagrangian phase would continue. Since the nodal mass is constant during the Lagrangian phase, Eqs. (13) and (14) are used here to calculate the constant nodal mass.

The advantages of the intersection based remapping are obvious. Firstly, the volume fraction and material centroid in the new grid cells are directly calculated from the configurations of different materials from the old grid, rather than calculating the material flux. Hence it avoids the drawbacks of the flux based remapping like negative mass and unphysical material fragments in essence. Secondly, different from the flux based remapping where the new and old grid must be close to each other to calculate the appropriate flux region, the topology of the old and new grid can even be different in the intersection based remapping. This property significantly increases the flexibility in the rezoning phase.

The key technique of the intersection based remapping is an accurate, efficient and robust calculation of the intersection portion of any two arbitrary polyhedrons. This issue has been well settled by a robust and efficient polyhedron subdivision and intersection algorithm proposed by Chen et al. [52]. In their “Clipping and Projecting” algorithm, the instability in the small cut caused by the geometric degeneracy can be thoroughly avoided because the geometry integrity is preserved in the new algorithm. And they also report that their “Clipping and Projecting” algorithm improves the efficiency by 55% to 65%.

2.2. The MPM for structure

The computational cycle of the MPM consists of four primary steps: (1) particle-to-grid projection, (2) Lagrangian mesh momentum updating, (3) particle updating and (4) resetting the background grid. The formation of the MPM is analogical to the MMALE. In order to emphasize the similarity between the MPM and MMALE, the MPM is also presented by Lagrangian phase, rezoning phase and remapping phase.

2.2.1. Lagrangian phase

Spatial discretization. In the MPM, the body is discretized into particles as illustrated in Fig. 4.

The density can be approximated as

$$\rho(\boldsymbol{x}) = \sum_{p=1}^{n_p} m_p \delta(\boldsymbol{x} - \boldsymbol{x}_p) \tag{46}$$

where n_p is the total number of the particles, m_p is the mass of particle p, δ is the Dirac delta function with dimension of the inverse of volume, and $\boldsymbol{x}_p$ is the spatial coordinate of particle p. Step (1) is implemented by substituting Eq. (46) into Eqs. (7)∼(10), so that the mass, momentum, internal force and external force are obtained as

$$m^I = \sum_{p=1}^{n_{\mathrm{p}}} N_p^I m_p \tag{47}$$

$$p_i^I = \sum_{p=1}^{n_{\mathrm{p}}} N_p^I m_p v_{ip} \tag{48}$$

$$f_i^I = -\sum_{p=1}^{n_\mathrm{p}} V_p N_{p,j}^I \sigma_{ijp} \tag{49}$$

$$\tilde{f}_i^I = \sum_{p=1}^{n_\mathrm{p}} (m_p N_p^I b_{ip} + N_p^I \bar{t}_{ip} h^{-1} V_p) \tag{50}$$

where the subscript p denotes the variables associated with particle p, and m_p, V_p, σ_{ijp} and b_{ip} are the mass, volume, stress and body force per unit mass of particle p, respectively. $N_p^I = N^I\left(\boldsymbol{x}_p\right)$ is the shape function of the node I evaluated at the position of particle p. In Eq. (50), $\bar{t}_{ip} = \bar{t}_i(\boldsymbol{x}_p)$ is the traction of particle p and h is the thickness of the fictitious layer used to convert the surface integral into a volume integral.

Time integration. The leapfrog integration [73], a kind of central difference method which provides second-order accuracy in time integration, is used in the MPM in step (2). The velocity $v_i^{I,k+1/2}$ at time $t^{k+1/2}$ can be updated as

$$v_i^{I,k+1/2} = v_i^{I,k-1/2} + a_i^{I,k} \Delta t^k \tag{51}$$

where $a_i^{I,k}$ denotes the acceleration of node I at time t, which is derived from the nodal force, namely,

$$a_i^{I,k} = \frac{f_i^I + \tilde{f}_i^I}{m^I} \tag{52}$$

and then the displacement at time t^{k+1} can be updated as

$$u_i^{I,k+1} = u_i^{I,k} + v_i^{I,k+1/2} \Delta t^{k+1/2} \tag{53}$$

where

$$\Delta t^k = \frac{1}{2}(\Delta t^{k-1/2} + \Delta t^{k+1/2}) \tag{54}$$

After the momentum is updated on the background grid, the particle variables are then updated from the variables on the background grid in step (3), namely

$$\dot{\varepsilon}_{ijp}^{k+1/2} = \frac{1}{2}(N_{p,j}^I v_i^{I,k+1/2} + N_{p,i}^I v_j^{I,k+1/2}) \tag{55}$$

$$\dot{\Omega}_{ijp}^{k+1/2} = \frac{1}{2}(N_{p,j}^I v_i^{I,k+1/2} - N_{p,i}^I v_j^{I,k+1/2}) \tag{56}$$

$$v_{ip}^{k+1/2} = v_{ip}^{k-1/2} + \sum_{I=1}^{n_\mathrm{a}} N_p^I a_i^{I,k} \Delta t \tag{57}$$

$$x_{ip}^{k+1} = x_{ip}^k + \sum_{I=1}^{n_\mathrm{a}} N_p^I v_i^{I,k+1/2} \Delta t \tag{58}$$

where n_a, $\dot{\varepsilon}_{ij}$ and $\dot{\Omega}_{ij}$ are the total number of grid nodes, strain rate and vorticity rate respectively.

The constitutive model is used to update the stress from the strain rate and the vorticity rate which has been illustrated by Zhang [74] in detail. The MPM could update the particle stress at the beginning of each time step or at the end of each time step, which are referred to the update stress first scheme (USF), and the update stress last scheme (USL), respectively. In addition, the modified update stress last scheme (MUSL) which is an improvement over the USL can also be used in the MPM. The detailed solution scheme is illustrated in Fig. 5.

2.2.2. *Rezoning phase*

After step (3), all the information has been mapped back to particles, so that step (4) simply reset the deformed Lagrangian grid to its initial position. That is to say, the deformed grid is replaced by its original undeformed grid in rezoning phase, which does not take any extra cost. The structured hexahedron mesh is usually employed in 3D simulation.

2.2.3. *Remapping phase*

In the MPM, all physical variables are carried by particles. The physical variables of the new grid are reconstructed from those of particles at the beginning of the next time step by step (1). Therefore, the particles

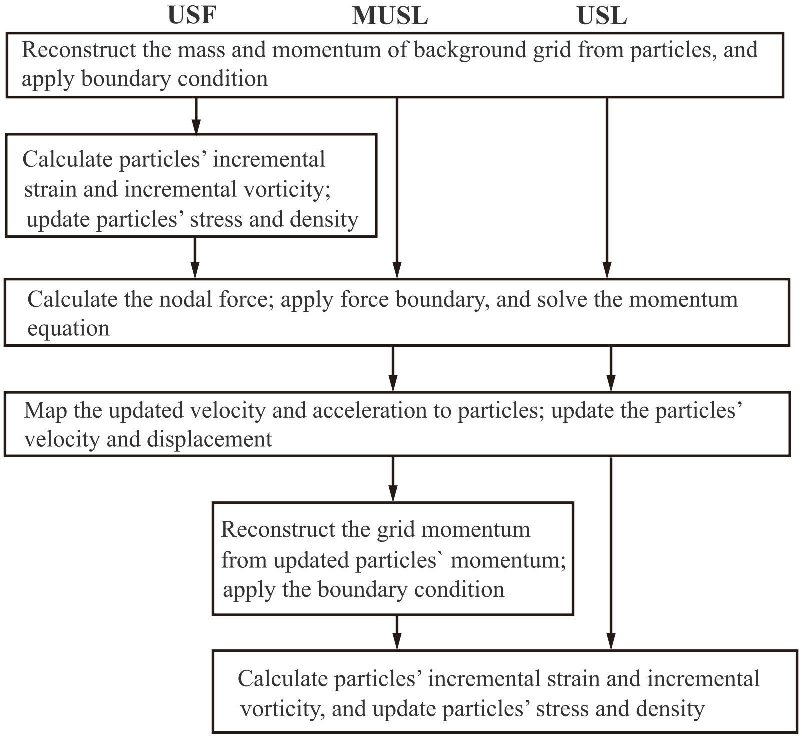

Fig. 5. Flow chart of the MPM [75].

take the role of intermedium to transmit information from the old grid to the new grid, and by this means, the MPM completes the remapping phase.

2.3. Comparison between the MMLAE and MPM

The MMALE and MPM both solve the weak form of momentum equation in an updating Lagrangian scheme with different spatial discretization and time integration schemes. The MMALE discretizes the calculation domain by a Lagrangian mesh, so that the accuracy is relatively higher and the problems with strong compression can be better simulated. The MPM stores all the information on the particles, so that the stress and strain histories for complex plastic material model are recorded in Lagrangian fashion without remapping dissipation, so that the MPM performs well in simulating the plastic deformation or structure damage. The MMALE is preferred in modeling multi-phase fluid flow, while the MPM is preferred in modeling the solid with extreme deformation and fracture. Therefore, it is a good choice to couple the MMALE and MPM to model the FSI problems with structure fracture.

Both the MMALE and MPM follow the same calculation framework of Lagrangian phase, rezoning phase and remapping phase. The difference is that in the MMALE, the rezoning and remapping phase are executed when mesh is distorted after plenty of Lagrangian steps, while in the MPM, the two Eulerian phases follow every Lagrangian step. Thus, it is very natural to couple the MMALE with MPM based on the immersed boundary technique to establish a monolithic FSI algorithm, as shown in next section.

3. Immersed multi-material arbitrary Lagrangian Eulerian material point method

Similar to the MMALE and MPM, the immersed multi-material arbitrary Lagrangian Eulerian material point method (IALEMPM) also consists of a Lagrangian phase, a rezoning phase and a remapping phase.

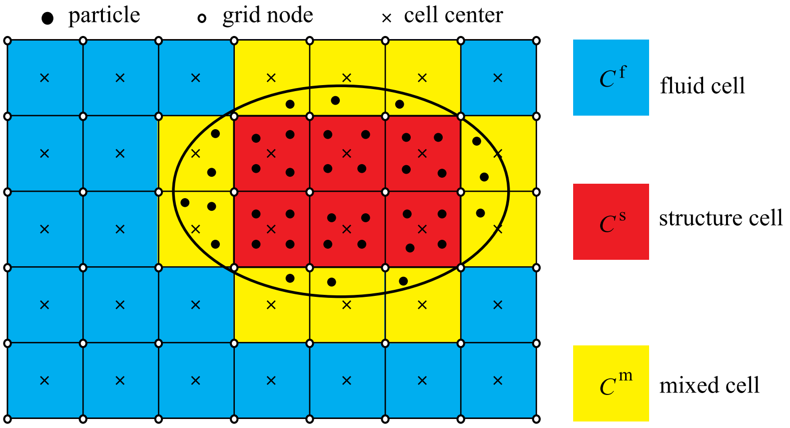

Fig. 6. The spatial discretization of the IALEMPM.

3.1. Lagrangian phase

Spatial discretization. The immersed boundary method is employed to develop the IALEMPM, in which the solid region is submerged in the fluid region, and the space occupied by solid domain is filled with the virtual fluid, as shown in Fig. 6. The fluid domain including the virtual fluid is discretized by a Lagrangian grid and the solid domain is discretized by a set of particles. The Lagrangian cells can be divided into three types, namely, fluid cells C^{f} occupied by fluid only, structure cells C^{s} occupied by solid only and the mixed cells C^{m} occupied partially by fluid and partially by structure. The weak form equation (4) is solved in the Lagrangian grid, so that the velocity, acceleration and displacement are stored on nodes. In the fluid cells, the density, pressure and internal energy are carried by the cell centers marked as "×" in Fig. 6. In the solid cell, the solid variables are carried by particles marked as solid dot, and the variables of virtual fluid are stored at the cell centers. For the mixed cell, the virtual and real fluids have the same physical variables stored in the cell center and the solid information are stored on the particles located in the cell.

In the solution domain, the density, stress and specific internal energy field can be described by

$$\rho = \rho^{\mathrm{f}} + \mu(\rho^{\mathrm{s}} - \rho^{\mathrm{f}}) \tag{59}$$

$$\sigma_{ij} = \sigma_{ij}^{\mathrm{f}} + \mu(\sigma_{ij}^{\mathrm{s}} - \sigma_{ij}^{\mathrm{f}}) \tag{60}$$

$$e = e^{\mathrm{f}} + \mu(e^{\mathrm{s}} - e^{\mathrm{f}}) \tag{61}$$

where

$$\mu(\boldsymbol{x}) = \begin{cases} 0 & \boldsymbol{x} \in \Omega^{\mathrm{f}} \\ 1 & \boldsymbol{x} \in \Omega^{\mathrm{s}} \end{cases} \tag{62}$$

with Ω^{f} denotes the fluid region and Ω^{s} denotes the solid region. These equations indicate that the solution domain could be treated as a fluid domain with a modification from the solid domain. Therefore, the integration in Eq. (8) can be calculated by integrating the fluid domain (including virtual fluid) variables and adding a solid particle integration modification, namely,

$$m^I = \int_{\Omega} \rho^{\mathrm{f}} N^I(\boldsymbol{x})\, \mathrm{d}\Omega + \int_{\Omega} \mu \left(\rho^{\mathrm{s}} - \rho^{\mathrm{f}}\right) N^I(\boldsymbol{x})\, \mathrm{d}\Omega \tag{63}$$

Combining Eqs. (13), (14) and (47) gives the nodal mass as

$$m^I = \sum_c \rho_c V_c^I + \sum_p \left(\rho_p - \rho_p'\right) V_p N_p^I \tag{64}$$

where the ρ_p' denotes the density of the virtual fluid in the support domain of particle p, and it is exactly the density of the structure cell or mixed cell in which the particle p locates. The right-hand side (RHS) of Eq. (64) contains a fluid part calculated by the cell-centered quadrature of MMALE and a solid modification part calculated by particle quadrature of MPM.

Similar to the nodal mass, the nodal force can be derived by substituting Eq. (60) into Eq. (9) and combining Eqs. (16) and (49), namely,

$$f_i^I = \sum_c f_{ci}^I - \sum_p V_p N_{p,j}^I \left(\sigma_{ijp} + P'_p \delta_{ij} \right) \tag{65}$$

where P'_p denotes the pressure of the virtual fluid which is located in the support domain of particle p. The nodal force in Eq. (65) still contains a fluid part calculated by the cell-centered quadrature of MMALE and a solid modification part calculated by particle quadrature of MPM. In the fluid cell, the nodal force is the same as the nodal force in the MMALE. In the structure cell, an error is derived from the different quadrature of the virtual fluid pressure. Compared with the fluid, the solid has much higher stiffness, so the virtual fluid pressure is much lower than the stress which makes the influence of the quadrature error can be neglected. However, in the mixed cell, also due to the high stiffness of the solid, the nodal force is mainly decided by the solid stress in Eq. (65), leading to the fluid flow changed by the solid stress. Hence, the fluid–structure interface is actually extended to the edge of mixed cell in the IALEMPM.

After the momentum is updated, the state variables on the cell centers (for fluid) and particles (for solid) are updated respectively. For the solid particles, the strain rate and vorticity rate are calculated by Eqs. (55) and (56). Then the stress is updated by a constitutive model. For the fluid cell centers, the energy conservation law is used to update the internal energy, and the pressure is updated by the internal energy. Substituting Eqs. (59)∼(61) into the energy conservation equation (3) leads to

$$\rho \frac{\mathrm{d}e}{\mathrm{d}t} = \rho^{\mathrm{f}} \frac{\mathrm{d}e^{\mathrm{f}}}{\mathrm{d}t} + \mu \left(\rho^{\mathrm{s}} \frac{\mathrm{d}e^{\mathrm{s}}}{\mathrm{d}t} - \rho^{\mathrm{f}} \frac{\mathrm{d}e^{\mathrm{f}}}{\mathrm{d}t} \right) = \dot{\varepsilon}_{ij} (\sigma_{ij}^{\mathrm{f}} + \mu (\sigma_{ij}^{\mathrm{s}} - \sigma_{ij}^{\mathrm{f}})) \tag{66}$$

Because the fluid and solid share a common displacement field, so the strain rate $\dot{\varepsilon}_{ij}$ between fluid and solid is the same. Integrating the equation in a cell and applying the cell center quadrature for fluid and particle quadrature for solid, the discrete energy equation in a cell is obtained as

$$\left(m_c - \sum_{p \in \Omega_c} \rho'_p V_p \right) \frac{\mathrm{d}e_c}{\mathrm{d}t} + \sum_{p \in \Omega_c} \rho_p V_p \frac{\mathrm{d}e_p}{\mathrm{d}t} = - \sum_I v_i^I f_{ci}^I + \sum_{p \in \Omega_c} \dot{\varepsilon}_{ijp} \sigma_{ijp} V_p + \sum_{p \in \Omega_c} \dot{\varepsilon}_{iicp} P'_p V_p \tag{67}$$

The energy conservation equation is satisfied on the particles, i.e.

$$\rho_p \frac{\mathrm{d}e_p}{\mathrm{d}t} = \dot{\varepsilon}_{ijp} \sigma_{ijp} \tag{68}$$

so that Eq. (67) can be rewritten by substituting $\dot{\varepsilon}_{ii}$ defined by Eq. (55) as

$$\left(m_c - \sum_{p \in \Omega_c} \rho'_p V_p \right) \frac{\mathrm{d}e_c}{\mathrm{d}t} = - \sum_I v_i^I f_{ci}^I + \sum_{p \in \Omega_c} \sum_I N_{p,i}^I v_i^I P'_p V_p \tag{69}$$

Comparing with Eq. (20) in MMALE, Eq. (69) subtracts the internal energy of the virtual fluid and makes a strict energy conservation. In pure fluid region, Eq. (69) is the same as Eq. (20). For the pure structure region, the mass of the real fluid calculated by the bracket in the LHS is zero. However the RHS is not essentially zero because the corner force in the MMALE is an approximation to center quadrature and is not equal to the particle quadrature in the MPM. Therefore, local instability may be introduced by Eq. (69).

Another choice to update the cell specific internal energy is to use the original equation (20) in the MMALE as an approximation. In the mixed and solid cells, Eq. (20) will bring in an energy error because the influence of the virtual fluid is not excluded in the energy calculation. But in solid region, the volume changes are always much lower than those in the fluid region due to the much higher stiffness of solid, so that the error is always quite low compared to the energy change in structure. As a result, Eq. (20) is more stable and efficient to update the fluid internal energy and is used to eliminate the potential local instability in this paper.

Time integration. The predictor–corrector scheme is used for the time integration, whose main process has been reviewed in Section 2.1.1.

For the predictor step, a temporary grid is first updated by Eqs. (21) and (22). The strain rate and vorticity rate of the structure are obtained as

$$\Delta\varepsilon_{ijp}^{k}=\frac{1}{2}\left(N_{p,j}^{I}v_{i}^{I,k}+N_{p,i}^{I}v_{j}^{I,k}\right)\cdot\frac{1}{2}\Delta t \tag{70}$$

$$\Delta\Omega_{ijp}^{k}=\frac{1}{2}\left(N_{p,j}^{I}v_{i}^{I,k}-N_{p,i}^{I}v_{j}^{I,k}\right)\cdot\frac{1}{2}\Delta t \tag{71}$$

and then the pressure $P_{c}^{k+1/2}$ and $\sigma_{ijp}^{k+1/2}$ are calculated by the isentropic hypothesis equation (23) and the constitutive model

$$\sigma_{ijp}^{k+1/2}=\sigma_{ij}\left(\sigma_{ijp}^{k},\Delta\varepsilon_{ijp}^{k},\Delta\Omega_{ijp}^{k}\right)$$

Substituting the temporary pressure and stress into Eq. (65) gives the nodal force f_i^I, and then substituting f_i^I into Eq. (24) gives the nodal acceleration.

For the corrector step, the grid of the next step is calculated by the temporary force and acceleration, namely Eqs. (25)∼(28). Then the cell centered variables for fluid are updated by Eqs. (29)∼(31). The variables on the particles for solid are updated by

$$\Delta\varepsilon_{ijp}^{k+1/2}=\frac{1}{2}\left(N_{p,j}^{I}v_{i}^{I,k+1/2}+N_{p,i}^{I}v_{j}^{I,k+1/2}\right)\Delta t$$

$$\Delta\Omega_{ijp}^{k+1/2}=\frac{1}{2}\left(N_{p,j}^{I}v_{i}^{I,k+1/2}-N_{p,i}^{I}v_{j}^{I,k+1/2}\right)\Delta t$$

$$\sigma_{ijp}^{k+1}=\sigma_{ij}\left(\sigma_{ijp}^{k},\Delta\varepsilon_{ijp}^{k+1/2},\Delta\Omega_{ijp}^{k+1/2}\right)$$

The solution scheme is briefly illustrated in Fig. 7. As the IALEMPM is a monolithic approach where the fluid and solid are solved together, there is no explicit displacement or force boundaries at the fluid structure interface. The FSI coupling process is implicitly implemented, and the fluid and solid are updated synchronously. In the Lagrangian phase, the fluid and structure region share the same displacement and velocity field. Therefore, the displacement continuity condition of FSI in all direction is automatically satisfied, which means that the IALEMPM adopts a no-slip boundary condition. In the inviscid flow which is focused in this paper, though the no-slip boundary imposes an additional restriction on the tangential velocity between the fluid and solid, this influence will only be restricted in one layer of fluid cell nearest the fluid–structure interface because the velocity gradient in the inviscid fluid will not cause tangential force. Therefore, the no-slip boundary is a valid approximation here. The interaction forces between solid and fluid are implicitly imposed by adding the nodal internal forces without tracking the fluid–structure interfaces.

In the Lagrangian phase, the Lagrangian solid particles move in accordance with the grid, which indicates that the nature coordinate of the particle in each cell is constant before the grid gets remeshed and the velocity of the particles can be directly interpolated from nodal velocities as

$$v_{ip}^{k}=\sum_{I}N_{p}^{I}v_{i}^{I,k} \tag{72}$$

where the shape function of particles is constant in time so denoted by N_p^I without superscript k. Due to this property, the particles in the Lagrangian phase could be treat as the quadrature point with fixed relative position to the grid.

The above formulation has no effect on the closure model, the artificial viscosity and the hourglass viscosity, so that the same technique for fluid computation is also applied in the IALEMPM.

It should be also noticed that in the IALEMPM, the algorithm only requires the solid to be inside the grid, no matter the grid element is void or not. So the solid can be correctly simulated when it is submerged in the void element. But when simulating the FSI problems with multiple materials, it is not practicable to set one kind of material as void element because the material interface with void material cannot be solved in fluid region. Taking the problem that structure enters the water as an example, the air part has to be set as air or other fluid instead of void because the void-water interface cannot be solved.

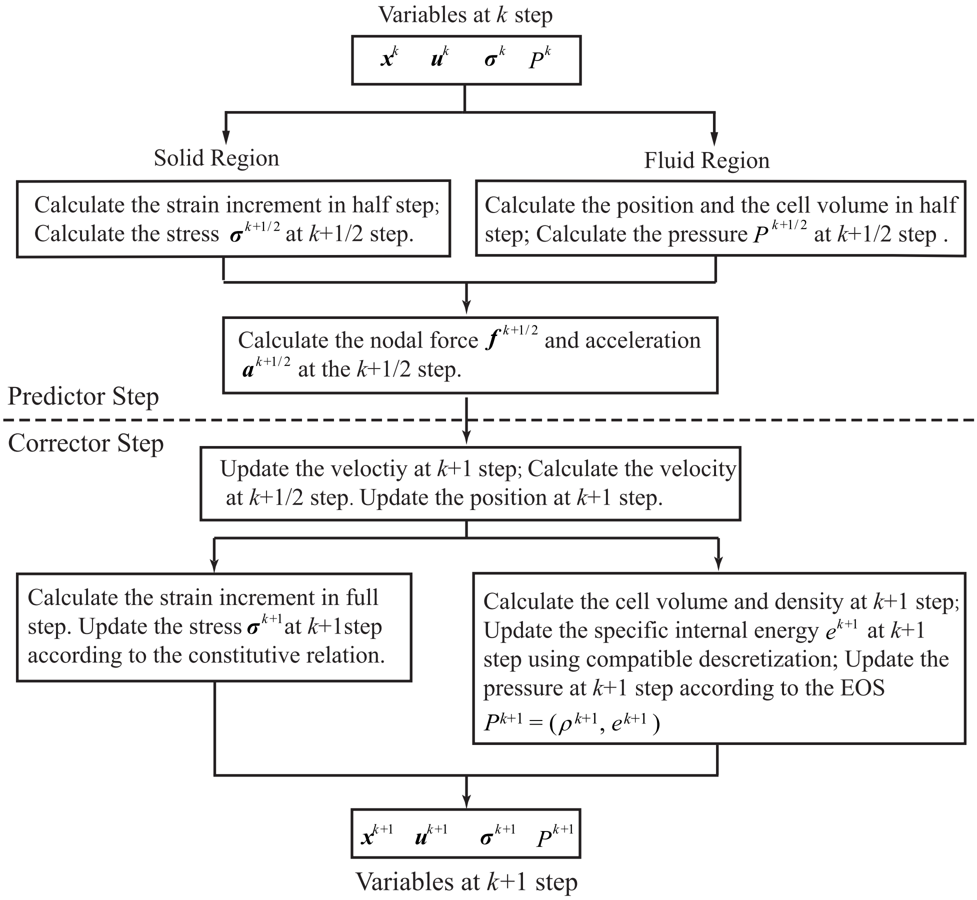

Fig. 7. Flow chart of the IALEMPM.

3.2. Rezoning phase

In the IALEMPM, the rezoning phase is essential to recover the grid quality. Because the grid is not required to conform the material interface or the fluid solid interface, any rezoning scheme can be used here according to the practical demand. One of the most convenient and efficient rezoning scheme is to recreate a structured regular hexahedron mesh for 3D simulation as the MPM does. In addition, a structured regular mesh makes the nature coordinate of particles in each cell easy to be determined.

3.3. Remapping phase

After the rezoning phase, the physical variables in the newly created domain are calculated from the old domain. In the remapping phase, variables from both the old grid and the particles should be taken into consideration. The process of the remapping phase of IALEMPM is illustrated in Fig. 8: (a) The old distorted grid contains real fluid region in blue and structure region in gray; (b) The fluid region containing the real fluid region and virtual fluid region in green is remapped to new grid by the intersection method described in Section 2.1.3. The rezoned grid is represented by black lines while the distorted old grid is represented by yellow lines; (c) The new grid is modified by solid properties on the particles (black dot).

Firstly, the remapping step of the fluid region uses the intersection method in MMALE. The cell-centered variables are calculated by accumulating in Eqs. (34)∼(38) and averaging in each cell as Eqs. (39)∼(42). The velocity field is calculated by intersecting the control domains of nodes, namely Eqs. (43)∼(45).

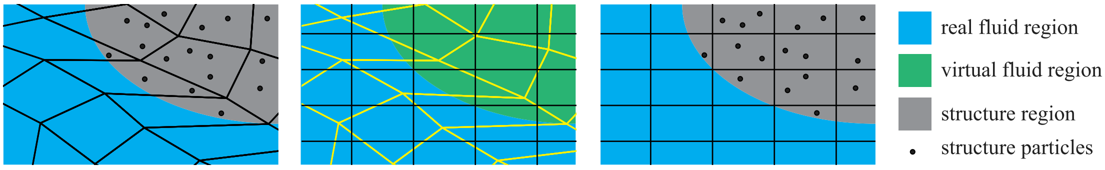

(a) (b) (c)

Fig. 8. Remapping process of IALEMPM. (For interpretation of the references to color in this figure legend, the reader is referred to the web version of this article.)

In order to modify the new grid by solid region, the nature coordinate of each particle is first calculated to derive the shape function $\tilde{N}_p^I$ in the new grid. The mass and momentum calculated by Eqs. (43) and (44) only allow for the contribution of fluid region without solid region, so that a modification should be applied here which is similar to the nodal mass and force modification, namely,

$$\tilde{m}^I = \sum_t \rho_t \int_{\Omega(H_t \cap \tilde{\Omega}_c)} \mathrm{d}\Omega + \sum_p (\rho_p - \rho_p') V_p \tilde{N}_p^I, \ \ t \in \{t \mid H_t \cap \tilde{\Omega}^I \neq \emptyset\} \tag{73}$$

$$\tilde{p}_i^I = \sum_t v_{ti} \rho_t \int_{\Omega(H_t \cap \tilde{\Omega}_c)} \mathrm{d}\Omega + \sum_p (\rho_p - \rho_p') v_{ip} V_p \tilde{N}_p^I, \ \ t \in \{t \mid H_t \cap \tilde{\Omega}^I \neq \emptyset\} \tag{74}$$

where ρ_p' denotes the density of the virtual fluid in old grid cell in which the particle p is located. Then the final velocity of the new grid can be calculated by Eq. (45).

Similar to the remapping phase in the MMALE, the nodal mass calculated by intersection in Eq. (73) is only to solve the nodal velocity, and then the constant nodal mass is calculated in this step by Eq. (64).

In this paper, the remapping algorithm is based on the work by Jia et al. [51] which has second order accuracy and the "Clipping and Projecting" intersection algorithm proposed by Chen et al. [52] which improves the efficiency by 55% to 65%. In both MMALE and IALEMPM, the remapping phase only carries out after the rezoning phase, so that there are lots of time steps between two remapping phases. However the remapping phase is still time consuming and accounts for more than 50% total simulation time in the examples in the next section. Therefore, improving the efficiency of the remapping phase is significant to the MMALE and IALEMPM.

4. Numerical examples

In this section, three numerical examples, including a 2D shock-obstacle interaction, a blast-plate interaction and a structure fragmentation under blast load, are studied to investigate the performance of the IALEMPM in modeling different kinds of problems.

4.1. 2D shock-obstacle interaction

The shock-obstacle interaction problem is an important field of research not only in fundamental sciences but also in engineering applications. In this simulation, the propagation, reflection and superposition of a shock wave under the influence of solid obstacle could be found, which will examine the capability of the IALEMPM to solve the compressible fluid flow with shock wave under solid influence. The problem has been studied numerically [76,77] and experimentally [78,79], which makes this problem an excellent benchmark.

The simulation domain is chosen as $[0, 15] \times [-3.5, 3.5] \times [-0.005, 0.005]$. The initial domain is split into two sub-domains Ω_1 with $l_1 = 7$ and Ω_2 with $l_2 = 8$, as shown in Fig. 9. The sub-domain Ω_2 contains stationary gas of $(\rho_2, e_2, \boldsymbol{v}_2) = (1, 2.5, \mathbf{0})$, while the gas in sub-domain Ω_1 has the property of $(\rho_1, e_1, \boldsymbol{v}_1) = (3.673715, 6.15552, (2.4198, 0, 0))$. Both the two sub-domains have the same material which is the ideal gas with the specific heat ratio $\gamma = 1.4$. A piston-like boundary condition defined by the inward velocity $\boldsymbol{v}_1$ is prescribed at the left boundary initially. A cylinder obstacle with a diameter of $d = 1$ is set at $l_3 = 9$. The above settings make a shock wave at the interface of Ω_1 and Ω_2 propagate toward the right part with a constant velocity $M_s = 2.81$ until the wave impinges on the cylinder obstacle.

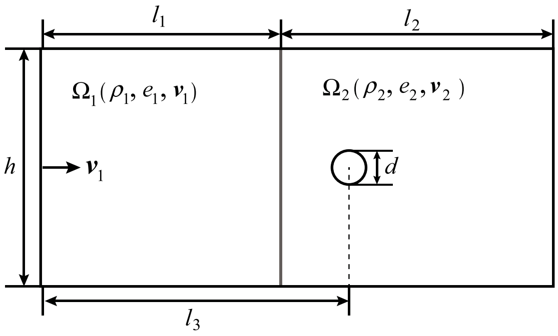

Fig. 9. Shock-obstacle interaction.

In the modeling of the ideal gas, the pressure is linear with the internal energy per unit initial volume E, namely,

$$P = (\gamma - 1)\frac{\rho}{\rho_0}E \tag{75}$$

where $E = \rho_0 e$. So the pressure on the pressure boundary at the right edge is set as $P_2 = 1$.

The Schlieren pictures obtained by the IALEMPM are compared with those obtained by experiment [79] in Fig. 10. In the early shock diffraction (Fig. 10(b)), the primary incident shock (IS), reflected bow shock (RS), first Mach shock (MS1), first contact discontinuity (CD1), vortex (V) and the first triple point (TP1) are well captured by the simulation. In the later diffraction (Fig. 10(d)), the second Mach shock (MS2), contact discontinuity (CD2) and triple point (TP2) can be easily identified. Compared to the experimental results of the two different times, the flow features are well simulated by the IALEMPM. Fig. 11 further compares the triple point trajectory obtained by the IALEMPM with those obtained by experiments [78,79]. This example shows that the simulation results of the IALEMPM are in good agreement with the experimental data.

The pressure time history of the diffraction process at several positions on the cylinder surface are plotted in Fig. 12(a). Seven gauge points are evenly set on the cylinder surface every 30 degrees. The shock wave could be captured by the pressure history. The peak pressure at the rear stagnation point 7 is higher than that of the point 5 and 6, which indicates a sudden jump of pressure after the two Mach shocks collide. The streamlines of the later shock diffraction are shown in Fig. 12(b). The formation of a pair of counter-rotating vortices together with the appearance of a curved reflected shock can be seen from the streamlines which is similar to the work by Chaudhuri et al. [77].

In general, the shock waves and the complex interactions under the influence of structure could be well captured and simulated by the IALEMPM.

4.2. Blast-plate interaction

In this example, a metal plate deforms under a blast load from a near-field explosion. This problem has been studied experimentally by Neuberger [80] with the devices shown in Fig. 13(a). They conducted series of experiments with different plate and explosive size, and recorded the maximal vertical displacement of the plate of each experiment. In this section, we simulate one of their experiments in order to examine the capability of the IALEMPM to solve problems with large structure deformation under fluid loading.

The solution domain is chosen as $[0\text{ m}, 0.3\text{ m}] \times [0\text{ m}, 0.3\text{ m}] \times [0\text{ m}, 0.15\text{ m}]$. The TNT explosive is located at the origin $(0\text{ m}, 0\text{ m}, 0\text{ m})$, and the plate is located at a distance of $R = 0.1$ m from the origin. Due to the symmetry, only the first octant of the model is simulated, as shown in Fig. 13(b). The TNT explosive is shown in blue, the plate is shown in red, and the air is shown in yellow. The surfaces of $x = 0$ m, $y = 0$ m and $z = 0$ m are set as symmetric boundaries, and the other three are set as pressure boundaries with the same pressure as the surrounding air. The diameter of the circular plate is $D = 0.5$ m with the thickness $d = 0.01$ m. The radius of the explosive is $r = 0.041$ m, so its mass is 0.468 kg.

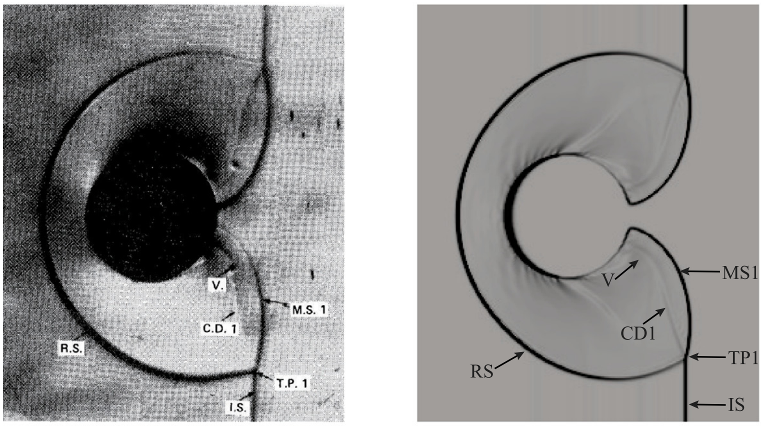

(a) Experiment: early shock diffraction (b) Simulation: early shock diffraction

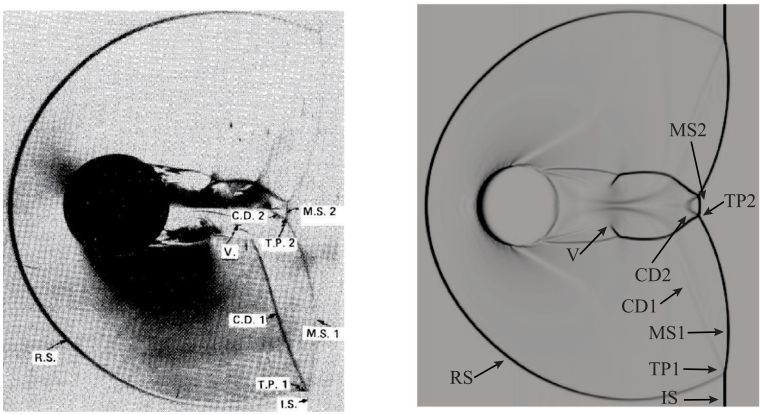

(c) Experiment: later shock diffraction (d) Simulation: later shock diffraction

Fig. 10. Schlieren picture obtained of experimental results [79] and IALEMPM.

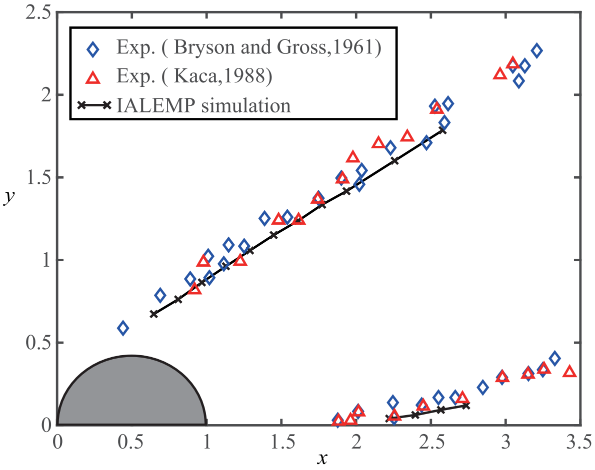

Fig. 11. Triple point trajectory (experimental data refers to Ref. [78,79]).

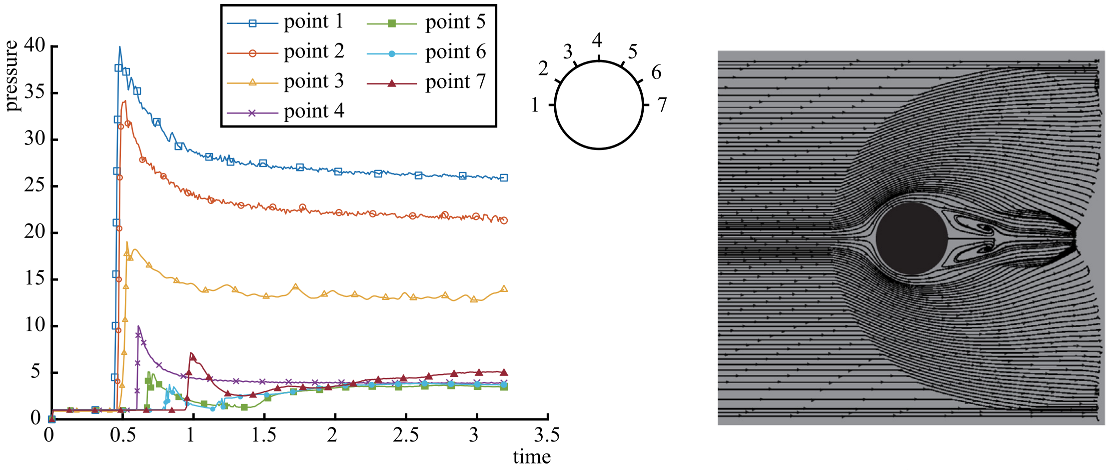

(a) (b)

Fig. 12. (a) Pressure history of gauge points; (b) Streamline.

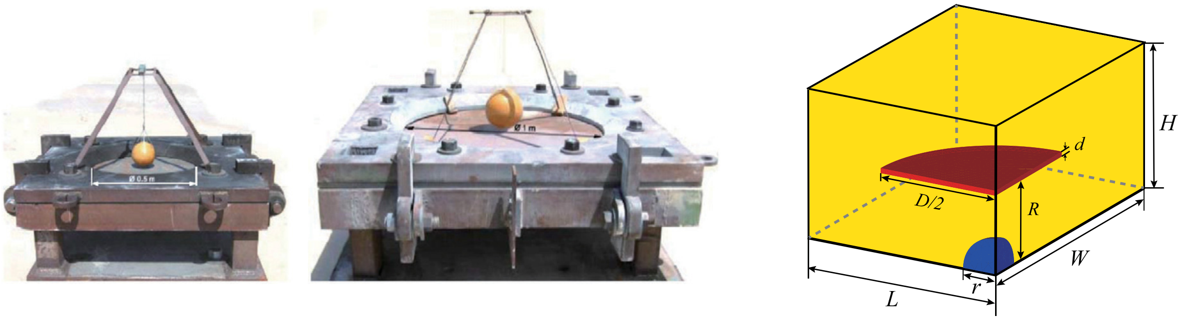

(a) (b)

Fig. 13. (a) The experiment devices [80] (b) Blast-plate interaction. (For interpretation of the references to color in this figure legend, the reader is referred to the web version of this article.)

The JWL equation of state

$$p = A\left(1-\frac{\omega}{R_1 V}\right)e^{-R_1 V} + B\left(1-\frac{\omega}{R_2 V}\right)e^{-R_2 V} + \omega\rho e \tag{76}$$

is used to model the explosive products [81], where $A = 3.7 \times 10^5$ MPa, $B = 3.23 \times 10^3$ MPa, $R_1 = 4.15$, $R_2 = 0.95$ and $\omega = 0.3$. $V = \rho_0/\rho$ is the relative volume. The initial density and the specific internal energy are $\rho_0 = 1630$ kg/m^3 and $e_0 = 4.3$ MJ/kg, respectively.

The circular plate is made of RHA steel which can be modeled by the simplified Johnson–Cook constitutive model [80]

$$\sigma_y = \left(A + B\varepsilon^{pn}\right)\left(1 + C\ln\dot{\varepsilon}\right) \tag{77}$$

where $A = 950$ MPa, $B = 560$ MPa, $n = 0.26$ and $C = 0.014$. The Young's modulus and Poisson's ratio of the RHA steel are 210 GPa and 0.28, respectively. The Mie–Gruneisen equation of state [82]

$$P = P_H\left(1-\frac{\gamma\mu}{2}\right) + \gamma\rho e \tag{78}$$

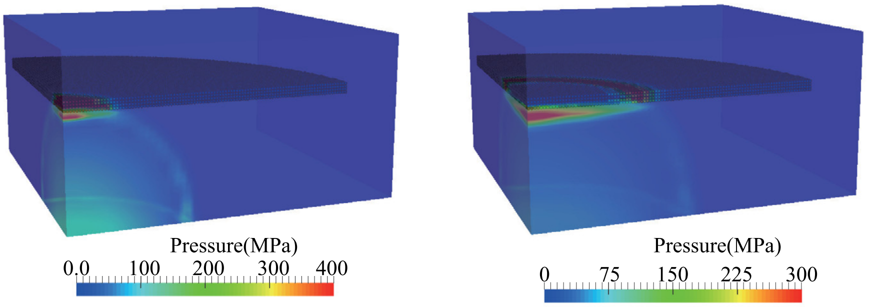

(a) t=0.024ms (b) t=0.034ms

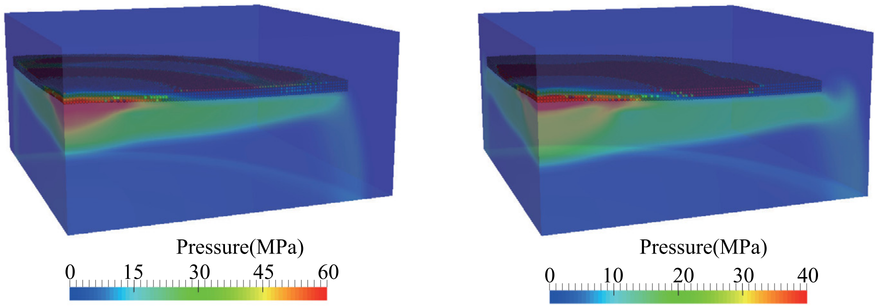

(c) t=0.072ms (d) t=0.088ms

Fig. 14. Fluid pressure contour.

is used to relate the state variables of RHA steel, where $\mu = \rho/\rho_0 - 1$ and $\gamma = 1.67$,

$$P_H = \begin{cases} \rho_0 C_0^2 \left[\mu + (2S-1)\mu^2 + (S-1)(3S-1)\mu^3\right] & \mu > 0 \\ \rho_0 C_0^2 \mu & \mu < 0 \end{cases} \tag{79}$$

with $\rho_0 = 7850\ \mathrm{kg/m^3}$, $C_0 = 4610$ m/s and $S = 1.49$.

The equation of the surrounding air is also the ideal gas equation modeled by Eq. (75) with initial density $\rho_0 = 1.225\ \mathrm{kg/m^3}$ and $e_0 = 0.2068$ MJ/kg. The terminate time is set as $t = 0.5$ ms before which the maximal vertical displacement of the plate has been reached.

Fig. 14 shows the pressure contour of the fluid region at different time before 0.1 ms. The solid is represented by particles. In this period, the shock wave generated from the explosion firstly propagates toward the plate. After the wave arrives at the plate, it interacts with the plate. For the fluid, the incident wave and reflected wave are superimposed and propagate along the radical direction of the plate with a higher peak pressure. For the plate, in the meantime, the stress wave is generated and the plate starts to deform gradually.

Fig. 15 shows the equivalent stress contour and deformation of the plate in a larger time scale until 0.5 ms. It shows that the deformation occurs at the center first and then expands along the radical direction. The magnitude of the equivalent stress increases gradually. In the experiment, the maximal displacement takes place at the center of the plate, and the ratio of the maximal displacement to the plate thickness $\delta_{\max}/d = 2.6$. Fig. 16 shows the displacement history of the plate center. The displacement increases until around 0.46 ms, and the ratio $\delta_{\max}/d$ turns out to be 2.44.

4.3. Structure fragmentation under blast load

4.3.1. Fragmentation of a cylinder shell

Tang et al. [83] observed the expanding fracture of 1045 steel cylinder shells driven by detonation using high speed photography. This experiment is studied here by the IALEMPM as a plain strain problem in order to examine the capability of the method to deal with structure fragmentation under the fluid loading. Due to symmetry, the simulation domain is chosen as [0, 75 mm] × [0, 75 mm] × [0, 0.25 mm] which contains a quarter concentric shell

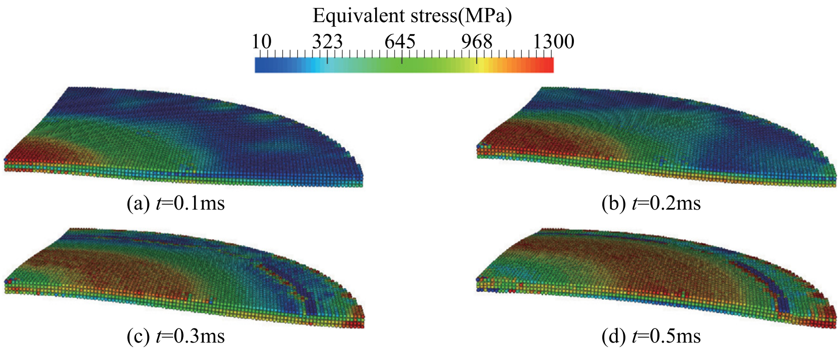

(a) t=0.1ms (b) t=0.2ms

(c) t=0.3ms (d) t=0.5ms

Fig. 15. Equivalent stress contour of the plate.

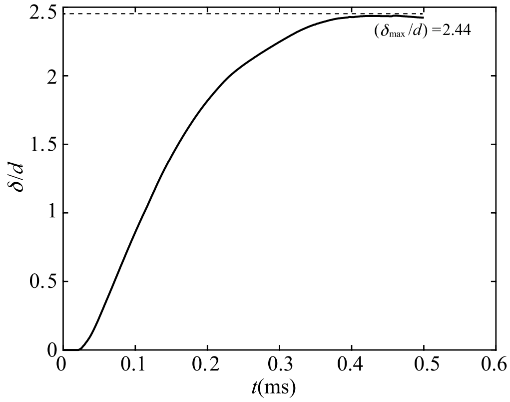

Fig. 16. Displacement history of the center.

Table 1
The constants of Gurson model [87].

q_1	q_2	f_{0e}	f_{0s}	f_f	f_c	f_N	ε_N	s_N	ε_p^f
1.5	1	0.005	0.0003	0.0021	0.2109	0.001	0.04	0.01	0.43

of TNT explosive and steel with two symmetric boundaries and two pressure boundaries with the same pressure as the surrounding air, as shown in Fig. 17. The inner radius and outer radius of the explosive are $r = 20$ mm and $R = 30$ mm respectively. The steel shell has thickness of $d = 4$ mm. The other part of the domain is the surrounding air. Three gauge points 1, 2 and 3 marked as yellow triangles are set with the distances $l_1 = 22$ mm, $l_2 = 25$ mm and $l_3 = 28$ mm, respectively to record the pressure histories.

In the experiment, the explosive is RHT-901 with a density of 1684 kg/m^3, and the parameters of JWL equation of state are taken from the literature [84] as $A = 524.2$ GPa, $B = 0.0321$ GPa, $R_1 = 4.15$, $R_2 = 0.95$, $w = 0.3$. For the steel, simplified Johnson–Cook model is used with $A = 5.07 \times 10^5$ MPa, $B = 3.2 \times 10^3$ MPa, $n = 0.28$, $C = 0.064$. The density of 7800 kg/m^3, Young's modulus of 210 GPa and Poisson's ratio of 0.3 are employed according to the literature [85]. In order to model the fragmentation, Gurson model [86] incorporated with a TEPLA-F failure condition which could describe the material microscopic defect under randomly distributed initial void fraction is employed here. From the experiment, the fracture strain of the shell is measured to be ε_p^f =0.43. So in the simulation, the parameters of the Gurson model and the TEPLA-F failure condition are listed in Table 1, where q_1, q_2, f_f, f_c, f_N, ε_N, and s_N are all parameters of Gurson model, f_{0e} and f_{0s} denote the mean and variance of the initial void fraction. The surrounding air is also treated as ideal gas.

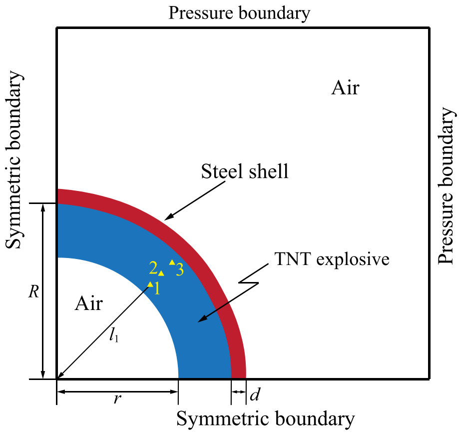

Fig. 17. Structure fragmentation under blast load.

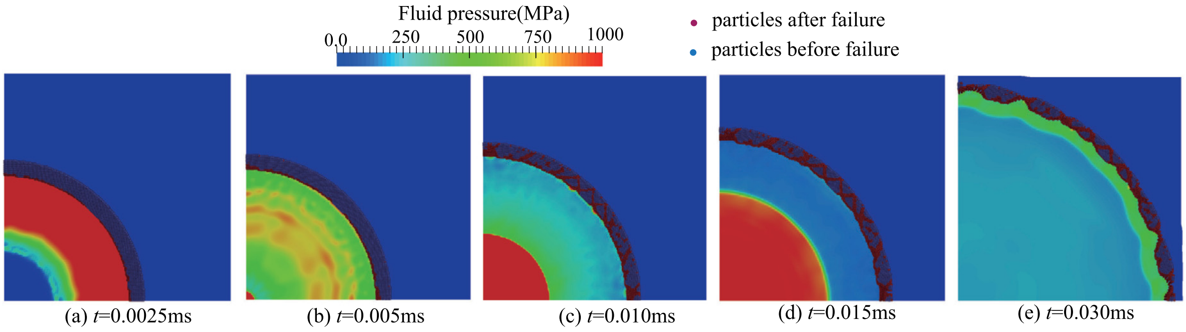

(a) t=0.0025ms (b) t=0.005ms (c) t=0.010ms (d) t=0.015ms (e) t=0.030ms

Fig. 18. Contour by the IALEMPM. (For interpretation of the references to color in this figure legend, the reader is referred to the web version of this article.)

Because the MPM can model both fluid and structure, this problem is also simulated by the MPM under the same simulation settings for comparison. The results obtained by the IALEMPM and MPM at different times are shown in Figs. 18 and 19 respectively, in which the fluid region is demonstrated by pressure contour, and the solid particles are colored by whether the particle is failed. The particles after failure are marked in red while those before failure are in blue. It shows that both the MPM and the IALEMPM reproduce the fracture process of the steel shell. The shear instability firstly occurs at the inner side of the shell where the material was compressed by detonation with high strain rate, causing particles here to fail. Then the outer side of the shell soon got in tension along the circumferential direction, leading to tensile fracture. When the tensile fracture at the outer side meet the shear instability band at the inner side, the mixed tensile-shear fracture grows up, which is indicated by the red cracks formed by failed particles. Nevertheless, the fracture simulated by the IALEMPM is more closed to the experimental result in terms of the appearance time of first crack, which is 8.0 μs in IALEMPM, 10.7 μs in MPM and 8.8 μs in the experiment reported by Tang et al. [83].

The kinetic energy history of the steel shell and the pressure history of the three gauge points are shown in Fig. 20. The kinetic energy history indicates that the load from the explosive can be divided into three stages. At the first stage, the steel shell suffers from the instantaneous blast pressure load. After a while, the explosive flows inside into the hollow cavity, leading to an unload to the shell. Finally, after a longer period of time, a shock wave reflected from the center crashes into the steel shell and make the third stage of the kinetic energy rise. The reflecting shock waves are captured clearly in the pressure history of gauge points in Fig. 20(b), (c) and (d) in the simulation by IALEMPM. However, in the curves of the MPM, the peak pressure is not sharp or clear in (c) and (d), as well as mass of oscillations can be found. This indicates that the IALEMPM perform much better in simulating the fluid region. In Fig. 20(a), a box named "fracture box" is plotted to show the period of time from the cracks

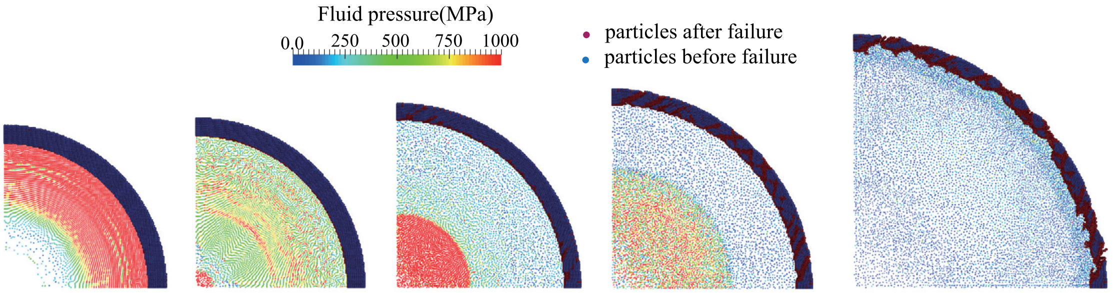

(a) t=0.0025ms (b) t=0.005ms (c) t=0.010ms (d) t=0.015ms (e) t=0.030ms

Fig. 19. Contour by the MPM. (For interpretation of the references to color in this figure legend, the reader is referred to the web version of this article.)

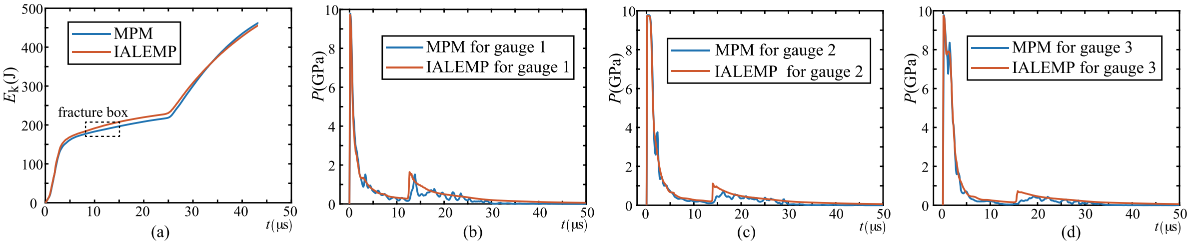

Fig. 20. Comparison between MPM and IALEMPM: (a) is the kinetic energy of steel shell, (b), (c) and (d) are pressure history of gauge 1, 2 and 3 respectively.

occurring to the stable crack patterns finally taking shape. The cracks are generated by the pressure loads, so that in the IALEMPM, a better simulation of fluid region derives a larger kinetic energy and acquires a more accurate occurrence time of the first crack.

4.3.2. Fragmentation of a sphere shell

The simulation of fragmentation of cylinder shell in Section 4.3.1 is extended to the fragmentation of a 3D sphere shell in this section. An 1/8 model of the sphere shell and TNT explosive are submerged in the surrounding air domain of [0, 50 mm] × [0, 50 mm] × [0, 50 mm], as illustrated in Fig. 21. The inner and outer radii of TNT are $R = 30$ mm and $r = 20$ mm, respectively. The thickness of the shell is $d = 4$ mm. The material of TNT, air and shell are set the same as those in Section 4.3.1.

In Fig. 22, the pressure contours in different time are shown in the left column. The propagation and reflection of the 3D spherical wave are clearly observed, which has the same three stages as those in the cylinder blast. The right column of the figure illustrates the creation of cracks and fragmentation of the shell, which is represented by particles. Under the blast loading, the shell is expanded, and the failed particles (shown in red) form the cracks.

A power-law distribution of the fragments was observed by Oddershede et al. [88]. The scaling exponent was found to be fairly sensitive to the shape of the object, but independent of the specific material, which can be interpreted as a self-organized critical phenomena [89]. The mass distribution of fragments follows a power-law, namely $n(m) \propto m^{-\beta}$ where n denotes the number of fragments with mass m and β is the shape parameter. The distribution of the fragments can be described by the total number of fragments with mass larger than or equal to m divided by m, namely

$$N(m) = \frac{1}{m} \int_m^{\infty} n\left(m'\right) \mathrm{d}m' \tag{80}$$

which is plotted in Fig. 23 for this example. It shows that the fragment distribution follows the power law with the parameter $\beta = 1.05$. Oddershede et al. [88] have found that the parameter β is 1.63 for solid spherical balls and 1.08 for thin disks. The sphere shell here is more like a disk, so that the obtained parameter $\beta = 1.05$ in this problem is reasonable and could verify the capacity of the IALEMPM in simulating fragmentation problems.

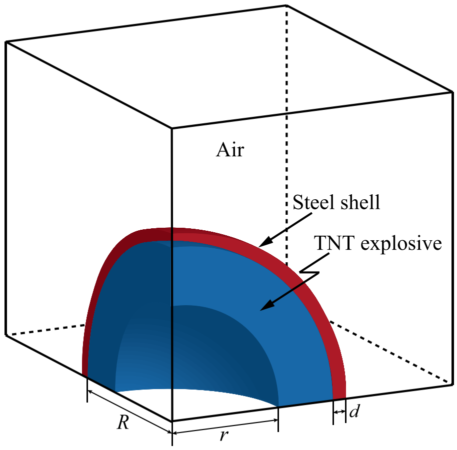

Fig. 21. 3D sphere fragmentation.

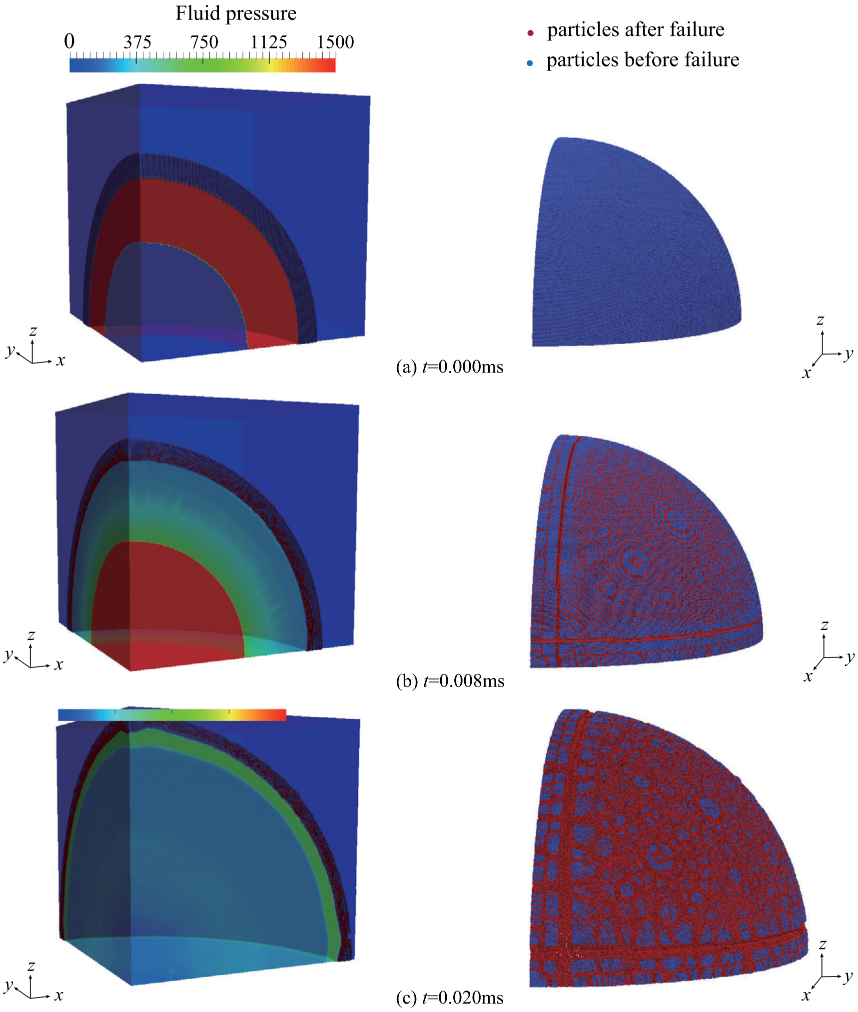

(a) *t*=0.000ms

(b) *t*=0.008ms

(c) *t*=0.020ms

Fig. 22. Pressure contour and shell fragmentation. (For interpretation of the references to color in this figure legend, the reader is referred to the web version of this article.)

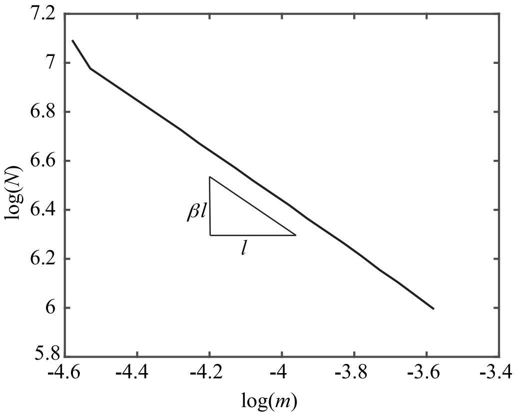

Fig. 23. Fragments distribution.

5. Conclusion

In this paper, a monolithic immersed multi-material arbitrary Lagrangian Eulerian material point method (IALEMPM) is proposed to solve the FSI problems with multi-material fluid flow and extreme structure deformation accompanied with fractures and crack growth. This novel method is established based on the framework of the MMALE which performs excellent in simulating multi-material flow and employs the particle quadrature and the particle discretization from the MPM which is superior in simulating structure damage and large deformation.

In the IALEMPM, the immersed method is introduced by setting the solid region submerged in the fluid region, and the space occupied by solid domain is filled with the virtual fluid. The fluid domain including the virtual fluid is discretized by a Lagrangian grid and the solid domain is discretized by material particles. The term “monolithic” is embodied in that the momentum equation of all the region is solved in the Lagrangian grid and the velocity and the displacement are continuous in both fluid and solid region. The fluid–structure interaction is implicitly implemented by assembling the nodal force and the nodal momentum from both the solid particles and fluid cells. This implicit interaction has no need to tack the complex fluid structure interface explicitly, hence the method is concise and applicable for engineering problems with extreme deformation and fractures. Besides, the consistent time integration scheme, rezoning phase and remapping phase are also established to guarantee the coincidence requirement in the whole simulation.

Three kinds of numerical tests are discussed to assess the performance of the IALEMPM. The 2D shock-obstacle interaction examines the capability of simulating the propagation, reflection and superposition of shock waves under solid influence. The blast-plate interaction examines capability of solving the large structure deformation under the fluid load, and the structure fragmentation test could examine the capability of simulating the structure fragmentation. The numerical results fit well with the benchmark and the experimental data, which indicates that the presented method is effective for solving the complicated FSI problems.

Declaration of competing interest

The authors declare that they have no known competing financial interests or personal relationships that could have appeared to influence the work reported in this paper.

References

[1] K. Khanafer, K. Vafai, A critical review on the applications of fluid–structure interaction in porous media, Internat. J. Numer. Methods Heat Fluid Flow (2020).
[2] S. Bandara, K. Soga, Coupling of soil deformation and pore fluid flow using material point method, Comput. Geotech. 63 (2015) 199–214.
[3] M. Bukač, S. Čanić, J. Tambača, Y. Wang, Fluid–structure interaction between pulsatile blood flow and a curved stented coronary artery on a beating heart: A four stent computational study, Comput. Methods Appl. Mech. Engrg. 350 (2019) 679–700.
[4] M. Ravensbergen, T. Helgedagsrud, Y. Bazilevs, A. Korobenko, A variational multiscale framework for atmospheric turbulent flows over complex environmental terrains, Comput. Methods Appl. Mech. Engrg. 368 (2020) 113182.

[5] G. Li, J. Gao, P. Wen, Q. Zhao, J. Wang, J. Yan, A. Yamaji, A review on mps method developments and applications in nuclear engineering, Comput. Methods Appl. Mech. Engrg. 367 (2020) 113166.
[6] Q. Zhu, F. Xu, S. Xu, M.-C. Hsu, J. Yan, An immersogeometric formulation for free-surface flows with application to marine engineering problems, Comput. Methods Appl. Mech. Engrg. 361 (2020) 112748.
[7] V. Kalro, T.E. Tezduyar, A parallel 3d computational method for fluid–structure interactions in parachute systems, Comput. Methods Appl. Mech. Engrg. 190 (3/4) (2000) 321–332.
[8] K. Stein, R. Benney, V. Kalro, T.E. Tezduyar, J. Leonard, M. Accorsi, Parachute fluid–structure interactions: 3-d computation, Comput. Methods Appl. Mech. Engrg. 190 (3–4) (2000) 373–386.
[9] T. Tezduyar, Y. Osawa, Fluid–structure interactions of a parachute crossing the far wake of an aircraft, Comput. Methods Appl. Mech. Engrg. 191 (6–7) (2001) 717–726.
[10] T.E. Tezduyar, S. Sathe, R. Keedy, K. Stein, Space–time finite element techniques for computation of fluid–structure interactions, Comput. Methods Appl. Mech. Engrg. 195 (17–18) (2006) 2002–2027.
[11] W. Kim, H. Choi, Immersed boundary methods for fluid–structure interaction: A review, Int. J. Heat Fluid Flow 75 (2019).
[12] C.W. Hirt, A.A. Amsden, J.L. Cook, An arbitrary lagrangian-eulerian computing method for all flow speeds, J. Comput. Phys. 14 (2) (1974) 227–253.
[13] J. Donea, S. Giuliani, J.P. Halleux, An arbitrary lagrangian-eulerian finite element method for transient dynamic fluid–structure interactions, Comput. Methods Appl. Mech. Engrg. 33 (1–3) (1982) 689–723.
[14] J.-L. Pfister, O. Marquet, M. Carini, Linear stability analysis of strongly coupled fluid–structure problems with the arbitrary-lagrangian-eulerian method, Comput. Methods Appl. Mech. Engrg. 355 (2019) 663–689.
[15] T.E. Tezduyar, Stabilized finite element formulations for incompressible flow computations, Adv. Appl. Mech. 28 (28) (1991) 1–44.
[16] B. Hübner, E. Walhorn, D. Dinkler, A monolithic approach to fluid–structure interaction using space–time finite elements, Comput. Methods Appl. Mech. Engrg. 193 (23–26) (2004) 2087–2104.
[17] S. Reinstädler, U. Kowalsky, D. Dinkler, Analysis of landslides employing a space–time single-phase level-set method, Comput. Methods Appl. Mech. Engrg. 347 (2019) 639–662.
[18] C.S. Peskin, Flow patterns around heart valves: A numerical method, J. Comput. Phys. 10 (2) (1972) 252–271.
[19] H.S. Udaykumar, W. Shyy, M.M. Rao, Elafint: A mixed eulerian-lagrangian method for fluid flows with complex and moving boundaries, Internat. J. Numer. Methods Fluids 22 (8) (2015) 691–712.
[20] T. Dunne, An eulerian approach to fluid–structure interaction and goal-oriented mesh adaptation, Internat. J. Numer. Methods Fluids 51 (9–10) (2010) 1017–1039.
[21] L. Zhang, A. Gerstenberger, X. Wang, W. Liu, Immersed finite element method, Comput. Methods Appl. Mech. Engrg. 193 (2004) 2051–2067.
[22] A. Neofytou, F. Yu, L.T. Zhang, H.A. Kim, Level set topology optimization for fluid–structure interactions, in: AIAA Scitech 2021 Forum, 2021.
[23] C. Jiang, J.-Y. Yao, Z.-Q. Zhang, G.-J. Gao, G. Liu, A sharp-interface immersed smoothed finite element method for interactions between incompressible flows and large deformation solids, Comput. Methods Appl. Mech. Engrg. 340 (2018) 24–53.
[24] C.E. Kees, J.H. Collins, A. Zhang, Simple, accurate, and efficient embedded finite element methods for fluid-solid interaction, Comput. Methods Appl. Mech. Engrg. 389 (2022) 114404.
[25] A. La Spina, M. Kronbichler, M. Giacomini, W.A. Wall, A. Huerta, A weakly compressible hybridizable discontinuous galerkin formulation for fluid–structure interaction problems, Comput. Methods Appl. Mech. Engrg. 372 (2020) 113392.
[26] L. Wang, C. Xie, W. Huang, A monolithic projection framework for constrained fsi problems with the immersed boundary method, Comput. Methods Appl. Mech. Engrg. 371 (2020) 113332.
[27] R.A. Gingold, J.J. Monaghan, Smoothed particle hydrodynamics: theory and application to non-spherical stars, Mon. Not. R. Astron. Soc. 181 (2) (1977) 375–389.
[28] T. Belytschko, Y.Y. Lu, L. Gu, Element-free Galerkin methods, Internat. J. Numer. Methods Engrg. 37 (2) (1994) 229–256.
[29] J.-S. Chen, C. Pan, C.-T. Wu, W.K. Liu, Reproducing kernel particle methods for large deformation analysis of non-linear structures, Comput. Methods Appl. Mech. Engrg. 139 (1–4) (1996) 195–227.
[30] S.G. Bardenhagen, J. Brackbill, D. Sulsky, The material-point method for granular materials, Comput. Methods Appl. Mech. Engrg. 187 (3–4) (2000) 529–541.
[31] S. Silling, Reformulation of elasticity theory for discontinuities and long-range forces, J. Mech. Phys. Solids 48 (1) (2000) 175–209.
[32] L. Han, X. Hu, SPH modeling of fluid–structure interaction, J. Hydrodyn. 30 (01) (2018) 62–69.
[33] Z.-F. Meng, A.-M. Zhang, J.-L. Yan, P.-P. Wang, A. Khayyer, A hydroelastic fluid–structure interaction solver based on the riemann-sph method, Comput. Methods Appl. Mech. Engrg. 390 (2022) 114522.
[34] M.N. Rahimi, D.C. Kolukisa, M. Yildiz, M. Ozbulut, A. Kefal, A generalized hybrid smoothed particle hydrodynamics-peridynamics algorithm with a novel lagrangian mapping for solution and failure analysis of fluid–structure interaction problems, Comput. Methods Appl. Mech. Engrg. 389 (2022) 114370.
[35] H. Fan, S. Li, A peridynamics-sph modeling and simulation of blast fragmentation of soil under buried explosive loads, Comput. Methods Appl. Mech. Engrg. 318 (2017) 349–381.
[36] A. Gilmanov, S. Acharya, A hybrid immersed boundary and material point method for simulating 3d fluid–structure interaction problems, Internat. J. Numer. Methods Fluids 56 (12) (2008) 2151–2177.
[37] P. Yu, K.S. Yeo, D. Shyam Sundar, S.J. Ang, A three-dimensional hybrid meshfree-cartesian scheme for fluid-body interaction, Internat. J. Numer. Methods Engrg. 88 (4) (2011) 385–408.
[38] Y. Liu, H. Ye, H. Zhang, Y. Zheng, Coupling lattice boltzmann and material point method for fluid-solid interaction problems involving massive deformation, Internat. J. Numer. Methods Engrg. 121 (24) (2020) 5546–5567.

[39] T. Shimada, K. Nishiguchi, R. Bale, S. Okazawa, M. Tsubokura, Eulerian finite volume formulation using lagrangian marker particles for incompressible fluid–structure interaction problems, Internat. J. Numer. Methods Engrg. http://dx.doi.org/10.1002/nme.6896, arXiv:https://onlinelibrary.wiley.com/doi/pdf/10.1002/nme.6896.

[40] P. Liu, Y. Liu, X. Zhang, Simulation of hyper-velocity impact on double honeycomb sandwich panel and its staggered improvement with internal-structure model, Int. J. Mech. Mater. Des. 12 (2) (2016) 241–254.

[41] S. Ma, X. Zhang, X. Qiu, Comparison study of MPM and SPH in modeling hypervelocity impact problems, Int. J. Impact Eng. 36 (2) (2009) 272–282.

[42] Z. Ma, X. Zhang, P. Huang, An object-oriented MPM framework for simulation of large deformation and contact of numerous grains, CMES - Comput. Model. Eng. Sci. 55 (1) (2010) 61.

[43] Y. Wang, H. Beom, M. Sun, S. Lin, Numerical simulation of explosive welding using the material point method, Int. J. Impact Eng. 38 (1) (2011) 51–60.

[44] J.A. Nairn, Material point method calculations with explicit cracks, Comput. Model. Eng. Sci. 4 (6) (2003) 649–663.

[45] H. Tan, J.A. Nairn, Hierarchical, adaptive, material point method for dynamic energy release rate calculations, Comput. Methods Appl. Mech. Engrg. 191 (19–20) (2002) 2123–2137.

[46] Y.-J. Cheon, H.-G. Kim, An adaptive material point method coupled with a phase-field fracture model for brittle materials, Internat. J. Numer. Methods Engrg. 120 (8) (2019) 987–1010.

[47] Y. Liang, B. Chandra, K. Soga, Shear band evolution and post-failure simulation by the extended material point method (xmpm) with localization detection and frictional self-contact, Comput. Methods Appl. Mech. Engrg. 390 (2022) 114530.

[48] Y.-P. Lian, Y. Liu, X. Zhang, Coupling of membrane element with material point method for fluid membrane interaction problems, Int. J. Mech. Mater. Des. 10 (2) (2014) 199–211.

[49] A.R. York, D. Sulsky, H.L. Schreyer, Fluid–membrane interaction based on the material point method, Internat. J. Numer. Methods Engrg. 48 (6) (2000) 901–924.

[50] J.S. Peery, D.E. Carroll, Multi-material ALE methods in unstructured grids, Comput. Methods Appl. Mech. Engrg. 187 (3/4) (2000) 591–619.

[51] Z. Jia, J. Liu, S. Zhang, An effective integration of methods for second-order three-dimensional multi-material ale method on unstructured hexahedral meshes using mof interface reconstruction, J. Comput. Phys. 236 (2013) 513–562.

[52] X. Chen, X. Zhang, Z. Jia, A robust and efficient polyhedron subdivision and intersection algorithm for three-dimensional mmale remapping, J. Comput. Phys. 338 (2017) 1–17.

[53] G. Clair, J.M. Ghidaglia, J.P. Perlat, A multi-dimensional finite volume cell-centered direct ale solver for hydrodynamics, J. Comput. Phys. 326 (2016) 312–333.

[54] F. Qing, X. Yu, Z. Jia, M. Qiu, X. Zhao, A high-order cell-centered discontinuous galerkin multi-material arbitrary lagrangian-eulerian method, Commun. Comput. Phys. 28 (4) (2020) 1464–1501.

[55] E.J. Caramana, D.E. Burton, M.J. Shashkov, P.P. Whalen, The construction of compatible hydrodynamics algorithms utilizing conservation of total energy, J. Comput. Phys. 146 (1) (1998) 227–262.

[56] M. Kenamond, D. Kuzmin, M. Shashkov, Intersection-distribution-based remapping between arbitrary meshes for staggered multi-material arbitrary lagrangian-eulerian hydrodynamics, J. Comput. Phys. 429 (2021) 110014.

[57] E.J. Caramana, C.L. Rousculp, D.E. Burton, A compatible, energy and symmetry preserving lagrangian hydrodynamics algorithm in three-dimensional cartesian geometry, J. Comput. Phys. 157 (1) (2000) 89–119.

[58] M. Shashkov, Closure models for multimaterial cells in arbitrary Lagrangian-Eulerian hydrocodes, Internat. J. Numer. Methods Fluids 56 (2008) 1479–1504.

[59] T. Kolev, R. Rieben, A tensor artificial viscosity using a finite element approach, J. Comput. Phys. 228 (2009) 8336–8366.

[60] E. Caramana, M. Shashkov, P. Whalen, Formulations of artificial viscosity for multi-dimensional shock wave computations, J. Comput. Phys. 144 (1998) 70–97.

[61] E. Caramana, M. Shashkov, Elimination of artificial grid distortion and hourglass-type motions by means of Lagrangian subzonal masses and pressures, J. Comput. Phys. 142 (1998) 521–561.

[62] A. Barlow, R. Hill, M. Shashkov, Constrained optimization framework for interface-aware sub-scale dynamics closure model for multimaterial cells in lagrangian and arbitrary lagrangian-eulerian hydrodynamics, J. Comput. Phys. 276 (2014) 92–135.

[63] D.J. Benson, Computational methods in lagrangian and eulerian hydrocodes, Comput. Methods Appl. Mech. Engrg. 99 (1992).

[64] Y.V. Yanilkin, E.A. Goncharov, V.Y. Kolobyanin, V.V. Sadchikov, W.J. Rider, Multi-material pressure relaxation methods for lagrangian hydrodynamics, Comput. & Fluids 83 (17) (2013) 137–143.

[65] R.E. Tipton, Cale mixed zone pressure relaxation, 1989, personal notes unpublished.

[66] M. Kucharik, R. Garimella, S.P. Schofield, M. Shashkov, A comparative study of interface reconstruction methods for multi-material ALE simulations, J. Comput. Phys. 229 (2010) 2432–2452.

[67] P. Knupp, L.G. Margolin, M. Shashkov, Reference jacobian optimization-based rezone strategies for arbitrary lagrangian eulerian methods, J. Comput. Phys. 176 (1) (2002) 93–128.

[68] H. Ahn, M. Shashkov, Multi-material interface reconstruction on generalized polyhedral meshes, J. Comput. Phys. 226 (2007) 2096–2132.

[69] X. Chen, X. Zhang, An improved 3D MoF method based on analytical partial derivatives, J. Comput. Phys. 326 (2016) 156–170.

[70] X. Chen, X. Zhang, An improved 2d mof method by using high order derivatives, J. Comput. Phys. 349 (2017) 176–190.

[71] J. Grandy, Conservative remapping and region overlays by intersecting arbitrary polyhedra, J. Comput. Phys. 148 (1999) 433–466.

[72] M. Kucharik, M. Shashkov, Conservative multi-material remap for staggered multi-material arbitrary-Lagrangian-Eulerian methods, J. Comput. Phys. 258 (2014) 268–304.

[73] P. Hut, J. Makino, S. Mcmillan, Building a better leapfrog, Agron. J. 443 (2) (1995) L93–L96.

[74] X. Zhang, Z. Chen, Y. Liu, The Material Point Method: A Continuum-Based Particle Method for Extreme Loading Cases, Academic Press, 2016.

[75] L. Kan, Y. Liang, X. Zhang, A critical assessment and contact algorithm for the staggered grid material point method, 2021.

[76] J.Y. Yang, Y. Liu, H. Lomax, Computation of shock wave reflection by circular cylinders, Aiaa J. 25 (5) (1987) 683–689.

[77] A. Chaudhuri, A. Hadjadj, A. Chinnayya, On the use of immersed boundary methods for shock/obstacle interactions, J. Comput. Phys. 230 (5) (2011) 1731–1748.

[78] J. Kaca, An interferometric investigation of the diffraction of a planar shock wave over a semicircular cylinder, in: Nasa Sti/Recon Technical Report N, 1988.

[79] A.E. Bryson, R. Gross, Diffraction of strong shocks by cones, cylinders, and spheres, J. Fluid Mech. 10 (01) (1961) 1–16.

[80] A. Neubergera, S. Peles, D. Rittel, Scaling the response of circular plates subjected to large and close-range spherical explosions. part i air-blast loading, Int. J. Impact Eng. 32 (2007) 859–873.

[81] M.B. Liu, G. Liu, K.Y. Lam, Meshfree particle simulation of the detonation process for high explosive in shaped unlined cavity configurations, Shock Waves 12 (6) (2003) 509–520.

[82] Meyers, Dynamic Behavior of Materials, John Wiley and Son, 1994.

[83] T. Tang, Y. Gu, Q. Li, J. Hua, X. Sun, Expanding fracture of steel cylinder shell by detonation drivings, Explos. Shock Waves 23 (6) (2003) 529–533.

[84] H.S. Dong, High Energy Explosive and Some Related Properties, Sceience Press, Beijing, 1989.

[85] G. Chen, Z. Chen, W. Xu, Y. Chen, X. Huang, Investigation on the J-C ductile fracture parameters of 45 steel, Explos. Shock Waves 27 (2) (2007) 131–135.

[86] L.A. Gurson, Continuum theory of ductile rupture by void nucleation and growth: Part I – Yield criteria and flow rules for porous ductile media, J. Eng. Mater. Technol. 99 (1) (1977) 297–300.

[87] X. Lin, S.C. Fong, Ductile crack growth – II. void nucleation and geometry effects on macroscopic fracture behavior, J. Mech. Phys. Solids 43 (12) (1995) 1953–1981.

[88] L. Oddershede, P. Dimon, J. Bohr, Self-organized criticality in fragmenting, Phys. Rev. Lett. 71 (19) (1993) 3107–3110.

[89] H. Inaoka, E. Toyosawa, H. Takayasu, Aspect ratio dependence of impact fragmentation, Phys. Rev. Lett. 78 (18) (1997) 3455–3458.